Targeted degradation of oncogenic KRAS^{G12V} triggers antitumor immunity in lung cancer models
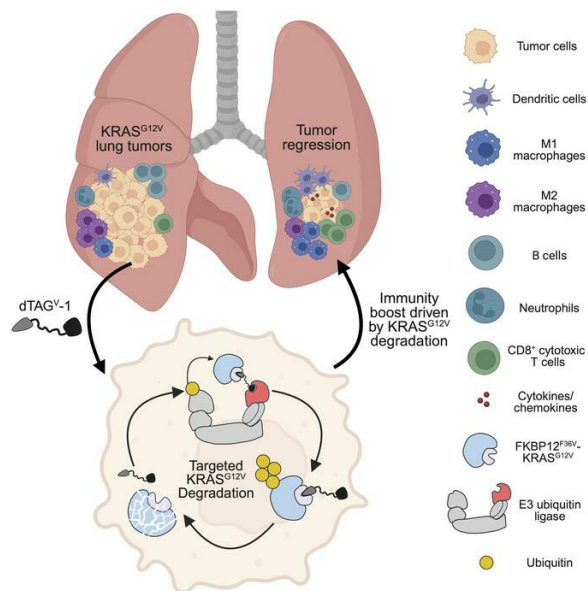
Dezhi Li, … , Kwok-Kin Wong, Hua Zhang

Research In-Press Preview Immunology Oncology

Graphical abstract

Targeted degradation of oncogenic KRAS^{G12V} triggers antitumor immunity in lung cancer models

Dezhi Li[1,19,#], Ke Geng[1,#], Yuan Hao[2,#], Jiajia Gu[3,#], Saurav Kumar[4,#], Annabel T. Olson[4], Christina C. Kuismi[4], Hye Mi Kim[3,5], Yuanwang Pan[1], Fiona Sherman[1], Asia M. Williams[3,5], Yiting Li[3,6], Fei Li[7,8], Ting Chen[1], Cassandra Thakurdin[1], Michela Ranieri[1], Mary Meynardie[1], Daniel S. Levin[1], Janaye Stephens[1], Alison Chafitz[1], Joy Chen[4], Mia S. Donald-Paladino[4], Jaylen M. Powell[1], Ze-Yan Zhang[9], ,Wei Chen[10], Magdalena Ploszaj[1], Han Han[1], Shengqing Stan Gu[11], Tinghu Zhang[12], Baoli Hu[3,13], Benjamin A. Nacev[3,14,15], Medard Ernest Kaiza[3,5], Alice H. Berger[4], Xuerui Wang[3,5], Jing Li[3,5], Xuejiao Sun[3], Yang Liu[16], Xiaoyang Zhang[17], Tullia C. Bruno[3,5], Nathanael S. Gray[12], Behnam Nabet[4,18*], Kwok-Kin Wong[1*], Hua Zhang[3,14*]

[1]Division of Hematology and Medical Oncology, Laura and Isaac Perlmutter Cancer Center, New York University Langone Health, New York, NY 10016, USA

[2]Applied Bioinformatics Laboratories, Office of Science and Research, New York University Grossman School of Medicine, New York, NY 10016, USA

[3]Hillman Cancer Center, UPMC, Pittsburgh, PA 15232 USA

[4]Human Biology Division, Fred Hutchinson Cancer Center, Seattle, WA 98109, USA

[5]Department of Immunology, University of Pittsburgh, Pittsburgh, PA 15261, USA

[6]School of Medicine, Tsinghua University, Beijing, China

[7]Department of Pathology, School of Basic Medical Sciences, Fudan University, Shanghai, China

[8]Frontier Innovation Center, School of Basic Medical Sciences, Fudan University, Shanghai, China

[9]Department of Radiation Oncology, New York University Grossman School of Medicine, New York, NY 10016, USA

[10]Division of Pulmonary Medicine, Department of Pediatrics, UPMC Children's Hospital of Pittsburgh and University of Pittsburgh, Pittsburgh, PA, USA

[11]Department of Hematopoietic Biology and Malignancy, University of Texas MD Anderson Cancer Center, Houston, TX, USA

[12]Department of Chemical and Systems Biology, Chem-H and Stanford Cancer Institute, Stanford School of Medicine, Stanford University, Stanford, CA 94305, USA

[13]Department of Neurological Surgery, University of Pittsburgh School of Medicine, Pittsburgh, PA 15261, USA

[14]Department of Medicine, Division of Hematology/Oncology, University of Pittsburgh School of Medicine, Pittsburgh, PA 15261, USA

[15]Department of Pathology, University of Pittsburgh School of Medicine, Pittsburgh, PA 15261, USA

[16]Department of Bioengineering, University of Illinois Urbana-Champaign, Urbana, IL 61801, USA

[17]Department of Oncological Sciences, Huntsman Cancer Institute, University of Utah, Salt Lake City, UT 84112, USA

41 [18]Department of Pharmacology, University of Washington, Seattle, WA 98195, USA

42 [19]Present address: Department of Pulmonary and Critical Care Medicine, Shandong Provincial
43 Hospital Affiliated to Shandong First Medical University, Jinan, 250021, China

44

46

47 #DL, KG, YH, JG, and SK contributed equally to this article.

48

49 *Corresponding Authors**: Hua Zhang, Hillman Cancer Center, UPMC, Department of Medicine,
50 Division of Hematology/Oncology, University of Pittsburgh School of Medicine, 5117 Centre
51 Avenue, Pittsburgh, PA 15261. Phone: 412-864-7742; Email: huz59@pitt.edu

52 Kwok-Kin Wong, Laura and Isaac Perlmutter Cancer Center, New York University Langone
53 Medical Center, 550 First Avenue, New York, NY 10016, USA. Phone: 212-263-9203; Email:
54 Kwok-Kin.Wong@nyulangone.org

55 Behnam Nabet, Human Biology Division, Fred Hutchinson Cancer Center, 1100 Fairview Avenue
56 N., Seattle, WA 98109, USA. Phone: 206-667-4052; Email: bnabet@fredhutch.org

57

Conflict-of-interest statement

72

Abstract

KRAS is the most frequently mutated oncogene in lung adenocarcinoma, with *G12C* and *G12V* being the most predominant forms. Recent breakthroughs in KRAS^{G12C} inhibitors have transformed the clinical management of patients with *G12C* mutation and advanced our understanding of its function. However, little is known about the targeted disruption of KRAS^{G12V}, partly due to a lack of specific inhibitors. Here, we leverage the degradation tag (dTAG) system to develop a *KRAS*^{G12V} transgenic mouse model. We explore the therapeutic potential of KRAS^{G12V} degradation and characterize its impact on the tumor microenvironment (TME). Our study reveals that degrading KRAS^{G12V} abolishes lung and pancreatic tumors in mice and causes a robust inhibition of KRAS-regulated cancer intrinsic signaling. Importantly, targeted degradation of KRAS^{G12V} reprograms the TME towards a stimulatory milieu and drives antitumor immunity, elicited mainly by effector and cytotoxic CD8$^+$ T cells. Our work provides important insights into the impact of degrading KRAS^{G12V} on both tumor progression and immune response, highlighting degraders as a powerful strategy for targeting *KRAS* mutant cancers.

Introduction

Non-small cell lung cancer (NSCLC) is one of the leading causes of cancer death worldwide (1). *KRAS* is the most frequently mutated oncogene in lung adenocarcinoma, the most common subtype of NSCLC (2). Approximately 30% of patients with lung adenocarcinoma harbor *KRAS* mutations, which are most commonly *G12C* and *G12V* (3). Directly targeting KRAS has been historically difficult until the recent development of KRAS^{G12C}-specific inhibitors including ARS-1620, AMG-510, and MRTX849 (4-7). These inhibitors have shown strong antitumor effects in *KRAS*^{G12C}-mutated lung adenocarcinoma preclinical models and patients (6, 8, 9). Notably, based on the positive clinical benefit observed in large clinical trials, the Food and Drug Administration (FDA) recently approved AMG-510 (Sotorasib) for the treatment of patients with KRAS^{G12C}-mutated NSCLC. Despite this remarkable breakthrough, Sotorasib demonstrates an approximately 30% response rate in patients with lung cancer (9, 10), with the rapid emergence of drug resistance (11-13). Furthermore, in stark contrast to the substantial advances in KRAS^{G12C} drug discovery, there are currently no approved specific inhibitors for KRAS^{G12V}. As drug discovery efforts focus on KRAS^{G12V}, an improved understanding of the biological consequences of KRAS^{G12V} disruption on tumor intrinsic signaling and the tumor microenvironment (TME) *in vivo* is necessary.

Targeted protein degradation has emerged as a powerful therapeutic approach to target oncogenic drivers (14-17). PROteolysis TArgeting Chimeras (PROTACs) are a class of small molecule degraders that bind a target protein and E3 ligase, leading to target protein ubiquitination and rapid proteasome-mediated degradation (18). PROTACs are advantageous over inhibitors due to their ability to abolish all protein activity including scaffolding functions (19, 20). We and others have endeavored to develop PROTACs to degrade KRAS^{G12C}, which has proven to be challenging (21, 22). While PROTACs such as LC-2 are capable of degrading KRAS^{G12C}, the benefits and liabilities of KRAS degradation *in vivo* remain unclear (22). Furthermore, although pan-KRAS degraders are in preclinical development (23-25) and KRAS^{G12D} degraders are in clinical trials (NCT05382559) (26), the consequences of targeted KRAS^{G12V} degradation in immune-competent models and the characterization of KRAS^{G12V}-selective degraders remain largely unexplored. Prior to the investment in the development of degraders, strategies to model the pharmacological degradation of drug targets are necessary.

As a solution to this challenge, we developed a versatile approach known as the degradation tag (dTAG) system to deplete tagged proteins *in vitro* and *in vivo* (27, 28). In this approach, a protein is expressed with an FKBP12^{F36V}-tag and is targeted for degradation using dTAG molecules that recruit an E3 ubiquitin ligase. We previously demonstrated that the dTAG system can be effectively employed to study the consequences of rapid and selective KRAS^{G12V} degradation in several cellular models (27-29). We and others have extensively applied the dTAG system to degrade diverse targets including oncoproteins, transcription factors, chromatin regulators, and kinases, illustrating the utility of the dTAG system for drug target validation and discovery (27, 28, 30, 31).

Mouse models are invaluable for understanding the biology of lung cancer, identifying potential therapeutic targets, and testing new treatments in a preclinical setting. Previous studies utilizing *KRAS*^{G12V} mouse models have advanced our understanding of KRAS^{G12V}-driven lung cancer and nominated new potential therapeutic approaches (32-35). In this study, to develop a platform for target drug validation *in vivo*, we advanced the dTAG system to establish a genetically engineered mouse model (GEMM) harboring *KRAS*^{G12V} amendable for specific and rapid degradation. This powerful model enabled us to comprehensively characterize the therapeutic potential of degrading KRAS^{G12V}. Utilizing this *KRAS*^{G12V} GEMM, we were able to dissect the tumor intrinsic responses as well as extrinsic effects including the impact on the TME upon degrading KRAS^{G12V}.

135 Our findings offer strong evidence for the promise of developing degraders targeting mutant
136 KRAS in cancer and also establish an *in vivo* platform for drug target discovery and validation.

137 **Results**

138 **Establishing a GEMM for targeted degradation of KRAS^{G12V} in lung cancer.**

139 Chemical-genetic degron strategies for achieving rapid, selective, and robust target protein loss
140 have emerged as powerful approaches for biological study and drug target validation (31, 36).
141 However, there are limited generalizable targeted degradation strategies available to study drug
142 target loss *in vivo*. KRAS^{G12V} is an ideal drug target to evaluate the consequences of targeted
143 degradation. Critically, the impact of KRAS^{G12V} protein degradation on tumorigenesis, intrinsic
144 signaling, and the TME is poorly understood, which is due to limited relevant mouse models and
145 specific KRAS^{G12V} inhibitors or degraders. To address these challenges, we set out to leverage
146 the dTAG system (27, 28) to establish a GEMM harboring *KRAS^{G12V}* amendable for specific and
147 rapid degradation (detailed in the Methods Section). In our approach, dTAG molecules bind an
148 FKBP12^{F36V}-tag and recruit an E3 ubiquitin ligase in proximity to induce FKBP12^{F36V}-fusion protein
149 degradation (**Figure 1A** and **Supplemental Figure 1A**). We previously demonstrated that our
150 dTAG molecules known as dTAG^V-1 and dTAG-13, which recruit von Hippel-Lindau (VHL) or
151 cereblon (CRBN), respectively, are selective and degrade KRAS^{G12V} in several cellular models,
152 including pancreatic ductal adenocarcinoma cell lines (27, 28). We also demonstrated that these
153 dTAG molecules display suitable pharmacokinetic (PK) and pharmacodynamic (PD) properties to
154 degrade tagged fusions in xenograft mouse models (27, 28, 37). Recent work has further
155 confirmed the tolerability of dTAG molecules *in vivo* and has shown that dTAG molecules
156 effectively degrade FKBP12^{F36V}-tagged proteins in embryonic stages of mouse development (38),
157 in several mouse organs (39), and patient-derived xenograft models (40).

158 Building on our prior work, we aimed to confirm that the FKBP12^{F36V}-KRAS^{G12V} protein is
159 functional and that it elicits comparable oncogenic responses to untagged KRAS^{G12V} *in vitro* and
160 *in vivo*. We first utilized NIH/3T3 cells, a commonly used model for testing oncogenic driver genes,
161 and expressed GFP or FKBP12^{F36V}-GFP as controls (**Figure 1B**), as well as KRAS^{G12V} and
162 FKBP12^{F36V}-KRAS^{G12V} (**Figure 1C**). The FKBP12^{F36V}-GFP and FKBP12^{F36V}-KRAS^{G12V} fusions
163 also include HA-tags to facilitate monitoring of GFP and KRAS^{G12V} levels. Importantly, comparable
164 hyperactivation of phosphorylated MEK (pMEK), a key component of oncogenic KRAS^{G12V}
165 downstream signaling, was observed upon the expression of KRAS^{G12V} and FKBP12^{F36V}-
166 KRAS^{G12V} (**Figure 1C**). We next confirmed the effectiveness of the recruitment of VHL to degrade
167 FKBP12^{F36V}-GFP or FKBP12^{F36V}-KRAS^{G12V} and reverse these responses. We observed that
168 dTAG^V-1 treatment resulted in the robust degradation of FKBP12^{F36V}-GFP (**Figure 1, B and C**)
169 and FKBP12^{F36V}-KRAS^{G12V} (**Figure 1C**), with no impact on untagged GFP or KRAS^{G12V} levels,
170 highlighting the specificity of dTAG^V-1 towards FKBP12^{F36V}-tagged fusions. The degradation of
171 FKBP12^{F36V}-KRAS^{G12V} rapidly reversed this aberrantly activated pMEK response back to baseline
172 levels (**Figure 1C**). Furthermore, dTAG^V-1-NEG, a control dTAG molecule that can bind to
173 FKBP12^{F36V} but not recruit VHL, did not degrade FKBP12^{F36V}-GFP or FKBP12^{F36V}-KRAS^{G12V} or
174 alter pMEK levels (**Figure 1, B and C**).

175 Next, we evaluated the oncogenic potential KRAS^{G12V} or FKBP12^{F36V}-KRAS^{G12V} *in vitro* and *in*
176 *vivo*. While NIH/3T3 cells expressing GFP or FKBP12^{F36V}-GFP were unable to proliferate as 3D-
177 spheroids, expression of KRAS^{G12V} or FKBP12^{F36V}-KRAS^{G12V} led to 3D-spheroid formation and a
178 significant growth advantage compared with their counterparts *in vitro* (**Figure 1D**). There was no
179 difference in the kinetics of 3D-spheroid formation between KRAS^{G12V} and FKBP12^{F36V}-KRAS^{G12V}
180 *in vitro* (**Figure 1D**). To further examine their tumorigenesis *in vivo*, NIH/3T3 cells expressing
181 KRAS^{G12V} or FKBP12^{F36V}-KRAS^{G12V} cells were injected subcutaneously into the flank of mice and
182 tumor volumes were measured. Consistently, the kinetics of tumorigenesis were comparable
183 between KRAS^{G12V} and FKBP12^{F36V}-KRAS^{G12V} *in vivo*, supporting that the FKBP12^{F36V}-tag did not
184 alter KRAS^{G12V} function (**Figure 1E**). Importantly, dTAG^V-1 treatment robustly diminished the
185 proliferation and viability of NIH/3T3 cells expressing FKBP12^{F36V}-KRAS^{G12V} (**Figure 1F**). With

186 our goal to evaluate targeted KRAS^{G12V} degradation in lung cancer models, we next confirmed
187 these observations in human lung epithelial cells (AALE) (**Supplemental Figure 1B**). We have
188 previously shown that KRAS^{G12V} transforms AALE cells and increases pMEK levels (41, 42).
189 Similar to the results with NIH/3T3 cells, compared to FKBP12^{F36V}-GFP, we observed that the
190 expression of FKBP12^{F36V}-KRAS^{G12V} in AALE cells led to elevated pMEK and the formation of 3D-
191 spheroids (**Supplemental Figure 1, B** and **C**). Pronounced degradation of FKBP12^{F36V}-KRAS^{G12V}
192 was observed upon treatment with dTAG^{V}-1, leading to a reversal of pMEK back to baseline and
193 diminished proliferation as 3D-spheroids (**Supplemental Figure 1, B** and **D**). Together, these
194 results support that the FKBP12^{F36V}-tag did not affect the functionality of the oncoprotein or alter
195 the kinetics of KRAS^{G12V}-induced tumorigenesis and validate the effectiveness of targeted
196 degradation of FKBP12^{F36V}-KRAS^{G12V} by dTAG^{V}-1.

197 These results motivated our development of a transgenic lung cancer mouse model that enables
198 specific degradation of FKBP12^{F36V}-KRAS^{G12V} using dTAG^{V}-1. We first designed a targeting
199 vector that included a PGK promoter and Lox-Stop-Lox cassette to allow for temporal and spatial
200 control of gene expression as we previously described (43) (**Figure 2A**). The transgene
201 expression is controlled by the Lox-Stop-Lox cassette which can be removed by Cre
202 recombinase. *FKBP12^{F36V}-KRAS^{G12V}* complementary DNA was cloned into the targeting vector
203 (**Figure 2A**). We also included HA-tags to enable monitoring of KRAS^{G12V} levels. After the
204 targeting vector was electroporated into mouse embryonic stem (ES) cells, these cells were
205 engineered to allow single-copy transgene insertion at the *Col1A1* locus. Mouse ES clones that
206 carry the *FKBP12^{F36V}-KRAS^{G12V}* transgene were selected, expanded, and used to inject into
207 C57BL/6 (B6) blastocysts, which gave rise to chimeras (**Figure 2A**). The chimeras were bred with
208 wild type B6 mice, and transgene-positive mice were genotyped, sequenced, and expanded for
209 experiments (**Figure 2B**).

210 We next sought to examine whether a single allele of *FKBP12^{F36V}-KRAS^{G12V}* would give rise to
211 lung adenocarcinoma modeling human disease in this model. *FKBP12^{F36V}-KRAS^{G12V}* mice were
212 induced by intranasal adenovirus-carrying Cre recombinase delivery at 6 to 8 weeks of age.
213 Starting from 12 to 14 weeks after the induction, *FKBP12^{F36V}-KRAS^{G12V}* mice had visible lung
214 tumors detected by MRI (**Figure 2C**). We then harvested mouse lungs from these *FKBP12^{F36V}-*
215 *KRAS^{G12V}* tumor-bearing mice to perform histologic analysis. Hematoxylin and eosin (H&E)
216 staining revealed the morphology of tumors formed by *FKBP12^{F36V}-KRAS^{G12V}* cells resembled
217 differentiated adenocarcinomas showing nuclear pleomorphisms including enlarged nuclei with
218 prominent nucleoli (**Figure 2D**) (44). Immunohistochemistry (IHC) staining of lung
219 adenocarcinoma-specific marker, TTF-1, demonstrated strong nuclear expression further
220 confirming primary pulmonary adenocarcinoma (**Figure 2D**). Our *FKBP12^{F36V}-KRAS^{G12V}* mouse
221 strain developed lung adenocarcinoma with complete penetrance and a consistent latency period,
222 comparable to previously reported *KRAS^{G12V}* models (32-35). In summary, we successfully
223 established an *FKBP12^{F36V}-KRAS^{G12V}* GEMM modeling the development of lung adenocarcinoma
224 and can be utilized for targeted degradation using the dTAG system.

225 **dTAG^{V}-1 effectively degrades KRAS^{G12V} and abolishes tumor growth in a *KRAS^{G12V}* GEMM.**

226 We next focused on evaluating the acute and prolonged responses to dTAG-mediated
227 degradation of FKBP12^{F36V}-KRAS^{G12V}. Based on our prior PK and PD studies (28), we treated a
228 cohort of *FKBP12^{F36V}-KRAS^{G12V}* tumor-bearing mice with 35 mg/kg of dTAG^{V}-1 continuously for
229 five days (formulation described in Supplemental Methods and performed as previously described
230 (28)), harvested tumor nodules, and evaluated FKBP12^{F36V}-KRAS^{G12V} degradation by monitoring
231 the HA-tag and downstream signaling (**Figure 3A**). Notably, we observed robust degradation of
232 FKBP12^{F36V}-KRAS^{G12V}, with a concomitant decrease in downstream pERK signaling by western
233 blotting and IHC staining (**Figure 3, B-D**). To examine the duration of FKBP12^{F36V}-KRAS^{G12V}
234 degradation *in vivo*, we treated a separate cohort of tumor-bearing mice with dTAG^{V}-1

235 continuously for five days. We then stopped compound administration and harvested tumors on
236 days 5 (2 hours after the last dose), 6, 7, and 8. Effective FKBP12^{F36V}-KRAS^{G12V} degradation
237 lasted for 72 hours following the last administration before returning to levels comparable to the
238 vehicle group (**Figure 3B** and **Supplemental Figure 2A**). These results demonstrate successful
239 target engagement and durable degradation of FKBP12^{F36V}-KRAS^{G12V} by dTAG^V-1. Furthermore,
240 we examined the antiproliferative and apoptotic effects upon abrupt FKBP12^{F36V}-KRAS^{G12V} loss
241 after five days of dTAG^V-1 treatment. IHC staining of the proliferation marker Ki-67 and apoptosis
242 marker cleaved caspase-3 showed that dTAG^V-1 led to a significant decrease in Ki-67 levels and
243 an increase in cleaved caspase-3 levels (**Figure 3, E** and **F and Supplemental Figure 2B**). We
244 next investigated the effects of acute FKBP12^{F36V}-KRAS^{G12V} degradation on extracellular matrix
245 component collagen using Masson's trichrome staining. Interestingly, dTAG^V-1 treatment caused
246 a reduction in collagen matrices in tumor-bearing lungs (**Supplemental Figure 2, C and D**),
247 suggesting a potential effect on tumor microenvironment upon FKBP12^{F36V}-KRAS^{G12V}
248 degradation.

249 After confirming that dTAG^V-1 successfully degraded FKBP12^{F36V}-KRAS^{G12V} and inhibited
250 oncogenic *KRAS* signaling, we proceeded to assess its impact on tumor growth in vivo. For this,
251 a separate cohort of *FKBP12^{F36V}-KRAS^{G12V}* GEMM mice was induced, and their tumor volumes
252 were monitored and quantified using MRI. Once tumor volumes reached approximately 100 mm^3,
253 mice were randomized into vehicle or dTAG^V-1 treatment groups (**Figure 4A**). All mice in the
254 vehicle group displayed aggressive disease progression after a 3-week period (**Figure 4, B and
255 C**). In contrast, mice treated with dTAG^V-1 showed a significant tumor response (**Figure 4, B and
256 C**), with MRI imaging revealing a reduction in tumor burden of over 50% in all treated mice after
257 long-term treatment by week 3 or week 4 (**Figure 4C**). Importantly, FKBP12^{F36V}-KRAS^{G12V}
258 degradation upon dTAG^V-1 administration dramatically increased the survival of tumor-bearing
259 mice (**Figure 4D**). These results indicate that KRAS^{G12V} degradation by dTAG^V-1 substantially
260 reduces tumor growth and prolongs survival in the *KRAS^{G12V}*-driven lung cancer model.

261 To extend these findings, we sought to validate the *in vivo* antitumor effects of KRAS^{G12V}
262 degradation in pancreatic cancer. To do so, we utilized an isogenic pancreatic ductal
263 adenocarcinoma cell line (PATU-8902 FKBP12^{F36V}-KRAS^{G12V}; *KRAS$^{-/-}$*) that we previously
264 developed to study KRAS^{G12V} degradation *in vitro* (29). We injected these cells subcutaneously
265 into the flank of nude mice. Once tumor volume reached approximately 100 mm^3, mice were
266 randomized to either vehicle or dTAG^V-1 treatment. Consistent with the results in our lung cancer
267 GEMM, degradation of KRAS^{G12V} upon administration of dTAG^V-1 significantly inhibited tumor
268 growth of PATU-8902 FKBP12^{F36V}-KRAS^{G12V}; *KRAS$^{-/-}$* cells (**Figure 4, E and F**). Collectively,
269 these findings validate the efficacy of KRAS^{G12V} degradation across different types of cancer and
270 support targeted degradation as an effective therapeutic strategy.

271 **KRAS^{G12V} degradation drives antitumor immunity through increasing CD8$^+$ T activity.**

272 Previous research has shown that KRAS inhibitors (AMG-510 and MRTX849) induce a pro-
273 inflammatory TME and achieve durable responses alone or in combination with immune
274 checkpoint inhibitors in pre-clinical mouse models (6, 45, 46). To investigate the immune
275 stimulatory effects of targeted degradation of KRAS^{G12V} *in vivo*, we profiled phenotypic and
276 functional alterations of CD8$^+$ T cells following a 5-day treatment with either vehicle or dTAG^V-1
277 in tumor-bearing mice (**Figure 5A**). T cells with high CD44 expression (effector/memory marker)
278 are characterized as effector cells, whereas T cells with high CD62L (naïve T cell marker) are
279 characterized as naïve cells. Profiling of CD8$^+$ T cells showed an increase of CD44^{high} effector
280 CD8$^+$ T cells and a decrease in CD62L^{high} naïve CD8$^+$ T cells upon KRAS^{G12V} degradation (**Figure
281 5, B and C**). To further assess the activation of CD8$^+$ T cells, we analyzed the expression of an
282 activation/co-stimulatory marker, CD69. KRAS^{G12V} degradation led to significantly higher
283 frequencies of CD69$^+$CD8$^+$ T cells (**Figure 5, D and E**). Additionally, we evaluated the activity of

284 cytotoxic T lymphocytes (CTLs) by staining for Granzyme B (GzmB), a cytotoxic granule protein
285 secreted by CD8$^+$ T cells. An increase in GzmB$^+$ CD8$^+$ T cells was observed upon FKBP12^{F36V}-
286 KRAS^{G12V} degradation, suggesting an enhanced cytotoxic T cell-mediated clearance of tumor
287 cells (**Figure 5, D** and **E**). These findings suggest that KRAS^{G12V} degradation stimulates a robust
288 antitumor immune program, potentially driven by activated CD8$^+$ T cells.

289 **Transcriptomic analysis reveals that KRAS^{G12V} degradation triggers immune response**
290 **signaling.**

291 To explore how KRAS^{G12V} degradation affects immune response signaling *in vivo*, we performed
292 a transcriptomic analysis on tumor nodules from mice treated with either vehicle or dTAG^V-1 for
293 5 days (**Supplemental Figure 3A**). Gene set enrichment analysis (GSEA) of differentially
294 expressed genes (dTAG^V-1 versus vehicle) identified the most modulated pathways
295 (**Supplemental Figure 3B**). FKBP12^{F36V}-KRAS^{G12V} degradation led to the downregulation of
296 genes associated with the cell cycle (**Supplemental Figure 3, B-D**), E2F targets (**Supplemental**
297 **Figure 3, E** and **F**) and mitosis (**Supplemental Figure 3, G** and **H**). Notably, FKBP12^{F36V}-
298 KRAS^{G12V} degradation led to the upregulation of pathways associated with the inflammatory
299 response, interferon gamma response, interferon alpha response, and allograft rejection
300 (**Supplemental Figure 3, I-L**). Heatmaps for the most differentially regulated genes in these top
301 signatures induced upon FKBP12^{F36V}-KRAS^{G12V} degradation showed an increased expression of
302 numerous central pro-inflammatory cytokines and chemokines, including *Tnf*, *Cxcl10* and *Ccl5*
303 (**Supplemental Figure 3M**). These factors secreted in the TME can potentially contribute to an
304 optimal antitumor T cell response. To confirm these findings, we then sought to measure the
305 expression of *CCL5*, *CXCL10* and *TNF* upon dTAG^V-1 treatment in AALE cells expressing
306 FKBP12^{F36V}-KRAS^{G12V} using quantitative reverse transcription-polymerase chain reaction (qRT-
307 PCR). dTAG^V-1 treatment significantly upregulated *CCL5* and *CXCL10*, with a trend towards
308 increased TNF expression (**Supplemental Figure 3N**). Furthermore, our RNA-seq data also
309 demonstrated that FKBP12^{F36V}-KRAS^{G12V} degradation increased the expression of numerous
310 granzyme subfamily members, including *Gmza*, *Gzmb*, *Gzmc*, as well as *Prf1* and *Ifng*
311 (**Supplemental Figure 3M**), which are crucial for CD8$^+$ T cell-mediated cytotoxicity. These
312 results, in line with immune profiling data, support the immune-stimulatory effects of KRAS^{G12V}
313 degradation.

314 **KRAS^{G12V} degradation reprograms the TME to enhance antitumor immunity.**

315 We next performed single-cell RNA-sequencing (scRNA-seq) to systematically examine the
316 impact on the TME upon degradation of KRAS^{G12V}. Lung tumors were collected after 5 days of
317 treatment with either vehicle or dTAG^V-1 to degrade FKBP12^{F36V}-KRAS^{G12V} in tumor-bearing
318 mice. We collected single suspension cells and sequenced them on the 10X Genomics platform.
319 In total, we obtained single-cell transcriptomes for 11,011 cells from the vehicle group and 7,486
320 cells from the dTAG^V-1 cohort. Using unsupervised clustering, we identified approximately 14
321 distinct cell clusters according to the gene expression signatures (**Figure 6A** and **Supplemental**
322 **Figure 4A**). We annotated these clusters with canonical cell type markers and identified tumor
323 cells expressing *Epcam* and *Nkx2-1*, B cells expressing *Cd19*, T cells expressing *Cd3d*, and NK
324 cells expressing *Ncr1*. We also identified various myeloid populations, including monocytes,
325 classical dendritic cells (cDCs), plasmacytoid DCs (pDCs) (marked by *Siglech*, *Bst2* and *Tlr7*),
326 monocyte-derived dendritic cells (marked by *Itgax*, *Flt3* and *Mgl2*), macrophages (both M1-like
327 and M2-like) and neutrophils (*S100a8*) (**Figure 6B** and **Supplemental Figure 4A**).

328 To dissect the TME alterations following KRAS^{G12V} degradation, we analyzed the immune cell
329 subpopulations. In comparison to the vehicle cohort, dTAG^V-1 administration slightly increased
330 the overall frequency of total immune cell populations (**Supplemental Figure 4B**). There was a
331 modest increase in the frequency of T cells, moDCs, NK cells, as well as innate lymphoid cells

332 (ILC) upon FKBP12^{F36V}-KRAS^{G12V} degradation (**Figure 6C**). Conversely, a decrease in the
333 percentages of B cells and monocytes was observed upon FKBP12^{F36V}-KRAS^{G12V} degradation
334 (**Figure 6C**). Macrophages are broadly classified into two main phenotypes based on their
335 activation states: classically activated (M1) and alternatively activated (M2) (47, 48). While M1-
336 like macrophages can exert antitumor effects, M2-like macrophages often contribute to tumor
337 growth and immune evasion (47, 48). Consistent with previous studies in the murine and human
338 lung tumors (49, 50), the macrophages in the lung TME largely belong to the M2-like
339 macrophages, expressing *Chil3* and *Mrc1* (**Supplemental Figure 4A**). Notably, our scRNA-seq
340 analysis revealed that dTAG^V-1 treatment led to an increase of M1-like macrophages expressing
341 *Ccl3*, *Tnf*, *Ler3*, *Clec4n*, *Tlr2/4* and *Cd80* (51), whereas a decrease in M2-like macrophages
342 expressing *Chil3* and *Mrc1* was observed (**Figure 6C** and **Supplemental Figure 4A**). The
343 reduction in M2-like macrophages was further validated by IHC staining of MRC1 (CD206) in the
344 lung tumors upon FKBP12^{F36V}-KRAS^{G12V} degradation (**Supplemental Figure 4, C** and **D**). These
345 findings suggest that KRAS^{G12V} degradation might have an impact on promoting tumor-associated
346 macrophages towards an M1-like antitumor phenotype. Given the high degree of heterogeneity
347 and plasticity of macrophages, further investigation and functional validation are warranted in
348 future work.

349 In addition, accumulating evidence indicates that B cells are strongly enriched in the TME in both
350 murine tumor models as well as human lung cancer patients (49, 52-54). In agreement with this,
351 our scRNA-seq analysis revealed B cells constitute a major immune cell population infiltrating in
352 the murine KRAS^{G12V} tumors. Unsupervised clustering of B cells identified four distinct clusters
353 (**Supplemental Figure 4E**). Consistent with recent findings (52), most tumor-infiltrating B cells
354 are in cluster 1, which exhibits a highly activated phenotype, expressing *Cd86* and *Cxcr4*. Cluster
355 2 B cells, expressing *Fcrl5*, display a memory-like phenotype (55, 56) (**Supplemental Figure 4F**).
356 Cluster 3 B cells, expressing *Hspa1a*, *Hspa1b*, and *Jun*, are associated with an activated
357 phenotype, whereas cluster 4, which is the smallest group, shows high expression of *Iglc1*
358 (**Supplemental Figure 4F**). Interestingly, FKBP12^{F36V}-KRAS^{G12V} degradation led to a decrease
359 in the percentage of cluster 1 B cells compared to the vehicle group, while the frequency of cluster
360 3 B cells increased (**Supplemental Figure 4G**). The percentages of clusters 2 and 4 remained
361 similar upon FKBP12^{F36V}-KRAS^{G12V} degradation. These observations suggest that KRAS^{G12V}
362 degradation differentially affects various subtypes of activated B cells, which merits further
363 investigation in the future.

364 Our *in vivo* immune profiling analysis suggested that KRAS^{G12V} degradation increased CD8$^+$ T
365 cell activity in the TME. To comprehensively characterize the T-cell subpopulations induced upon
366 FKBP12^{F36V}-KRAS^{G12V} degradation, we further analyzed the scRNA-seq dataset and performed
367 unbiased clustering of T cells. This approach identified 6 major clusters defined by the expression
368 of marker genes, suggesting heterogeneous and complex populations. In the CD8$^+$ T-cell
369 populations, cells with a high level of *Sell* and low levels of *Cd44* and *Ifng* are consistent with
370 naïve and inactivated states and were thus classified as 'CD8$^+$-naïve' cluster. FKBP12^{F36V}-
371 KRAS^{G12V} degradation reduced the percentage of naïve CD8$^+$ cells (**Figure 6, D-F**). Cells in
372 clusters with high *Ifng* and *Cd44* resemble cytotoxic T cells and effector T cells, which were
373 therefore classified as 'CD8$^+$-effector and cytotoxic T cells'. FKBP12^{F36V}-KRAS^{G12V} degradation
374 caused an increase in the effector and cytotoxic CD8$^+$ T cells (**Figure 6, D-F**). Additionally, in the
375 CD4$^+$ T-cell populations, we also observed a similar trend of decreased CD4$^+$-naïve T cells and
376 increased CD4$^+$-effector T cells (**Figure 6, D-F**). Our unbiased clustering also identified CD4$^+$
377 T$_{regs}$, which express high levels of *Foxp3* (**Figure 6, D-F**). An increase in the frequency of CD4$^+$
378 T$_{regs}$ was seen upon FKBP12^{F36V}-KRAS^{G12V} degradation, which might indicate potential feedback
379 from increased effector and cytotoxic T cell activity.

380 To complement our scRNA-seq findings of immune TME alterations, we performed multiplex
381 immunofluorescence (IF) analysis on lung tumors from mice that were subjected to a 5-day
382 treatment with either vehicle or dTAG^V-1 (**Figure 7, A-C**). Consistently, an increase of CD3$^+$ T
383 cells was observed upon abrupt loss of FKBP12^{F36V}-KRAS^{G12V}, compared with vehicle (**Figure 7,**
384 **A and C**). Likewise, dTAG^V-1 treatment also led to a higher percentage of Foxp3$^+$ T$_{regs}$ (**Figure 7,**
385 **A and C**). In addition, similar to our observations using scRNA-seq analysis, IF imaging showed
386 that the frequency of CD19$^+$ B cells was decreased upon FKBP12^{F36V}-KRAS^{G12V} degradation
387 (**Figure 7, B and C**).

388 In summary, in line with the *in vivo* immune profiling and bulk transcriptomic analysis, our scRNA-
389 seq analysis complemented with multiplex IF imaging confirms an antitumor immune response
390 following dTAG^V-1 treatment to degrade FKBP12^{F36V}-KRAS^{G12V}. These alterations include (1)
391 slightly increasing overall immune cell infiltration, (2) decreasing M2-like and increasing M1-like
392 macrophages, (3) decreasing B cells, (4) reducing the naïve CD8$^+$ and CD4$^+$ T cells, and (5)
393 increasing the effector and cytotoxic CD8$^+$ T cells. These data further support the beneficial effects
394 of targeted degradation of KRAS^{G12V} in rewiring the TME to enhance antitumor immunity.

395 **Antitumor immunity by KRAS^{G12V} degradation is partly dependent on CD8$^+$ T cells.**

396 Our integrated analysis above demonstrated that the antitumor immunity by KRAS^{G12V}
397 degradation centered on T cells. To determine whether CD8$^+$ or CD4$^+$ T cells directly contribute
398 to antitumor response by dTAG^V-1 treatment, we assessed the impact of perturbing immune cell
399 function by *in vivo* neutralization antibodies against CD8 (anti-CD8) or CD4 (anti-CD4)
400 (**Supplemental Figure 5**). FKBP12^{F36V}-KRAS^{G12V} tumor-bearing mice were randomized to
401 dTAG^V-1 treatment or combining dTAG^V-1 with either anti-CD8 or anti-CD4. Notably, compared
402 with non-depletion of T cells mice in the dTAG^V-1 group, CD8$^+$ T cell-depleted mice had
403 significantly higher tumor burdens (**Figure 7, D-F**). Interestingly, no significant difference was
404 observed between non-depletion mice and CD4$^+$ T cell-ablated mice (**Figure 7, D-F**). These
405 findings suggest depleting CD8$^+$ but not CD4$^+$ T cells mitigated the antitumor effect of FKBP12^{F36V}-
406 KRAS^{G12V} degradation by dTAG^V-1, highlighting antitumor immunity by KRAS^{G12V} degradation is
407 partly dependent on CD8$^+$ T cells.

408 In summary, our work offers valuable insights into how KRAS^{G12V} degradation influences both
409 tumor progression and the immune response, underscoring degraders as a potent strategy for
410 targeting *KRAS* mutant cancers. Furthermore, our study highlights the potential of the dTAG
411 system in developing GEMMs for the study and validation of drug targets.

Discussion

Targeted protein degradation holds incredible promise as a therapeutic strategy in diseases including cancer (14-17, 57). There is a current lack of targeted degradation strategies to study the consequences of drug target loss in $vivo$. Here, we focused on KRAS^{G12V}, which is the second most common mutation in NSCLC and a driver in several cancers including pancreatic and colorectal cancer (58, 59). While breakthroughs in the development of KRAS^{G12C} inhibitors including AMG-510 (Sotorasib) (9, 10, 60) and MRTX849 (Adagrasib) (61) represent a paradigm shift in the clinical management of NSCLC patients harboring a $KRAS^{G12C}$ mutation, there is currently a lack of selective $KRAS^{G12V}$ inhibitors. As the field moves towards targeting other additional KRAS mutants, an improved understanding of targeting KRAS^{G12V} in $vivo$ is necessary. We aimed to advance the dTAG system to generate a degradable cancer GEMM using KRAS^{G12V} as a prioritized target.

In this study, we demonstrate that this mouse model harboring a tagged allele of $KRAS^{G12V}$ recapitulates the development of human adenocarcinoma. Our $FKBP12^{F36V}$-$KRAS^{G12V}$ mouse strain develops lung adenocarcinoma with complete penetrance and a consistent latency period, comparable to previously reported $KRAS^{G12V}$ models (32-35). Critically, treatment with dTAG molecules effectively models the impact of targeted degradation of KRAS^{G12V}. In the mice, dTAG^{V}-1 administration led to robust and durable degradation of KRAS^{G12V}, along with pronounced inhibition of downstream signaling, consistent with previous findings from studies using KRAS inhibitors in murine cancer models (6, 7). Strikingly, dTAG^{V}-1 considerably reduced tumor growth in all treated $KRAS^{G12V}$ mice and the FKBP12^{F36V} tag did not affect the kinetics of KRAS^{G12V} transformation nor tumorigenesis in $vitro$ and in $vivo$. Furthermore, while we focused on developing an NSCLC GEMM, our incorporation of Cre-recombinase-mediated introduction of FKBP12^{F36V}-KRAS^{G12V} supports similar application in other tissues and cancers of interest including pancreatic cancer. Towards this aim, we performed experiments that extend into pancreatic cancer and demonstrate that dTAG^{V}-1-mediated KRAS^{G12V} degradation drastically inhibited tumor growth in the PATU-8902 pancreatic cancer model. Our study demonstrates the unique power of these mouse models for in $vivo$ evaluation of the effects of KRAS^{G12V} degradation on tumorigenesis.

Importantly, our GEMM enables the evaluation of responses in an immune-competent mouse, which led us to test whether degrading KRAS^{G12V} leads to an increased immune response in $vivo$. Prior work has linked KRAS^{G12C} inhibition to an immune response (46). In preclinical studies, treatment with AMG-510 showed a pro-inflammatory TME and induced durable cures alone, and in combination with immune-checkpoint inhibitors (6). Likewise, MRTX849 demonstrated an enhanced antitumor immunity, partly through increased MHC class I protein expression and decreased levels of immunosuppressive factors (45). MRTX849 also sensitized tumors to immune-checkpoint inhibitors (45). Like these observations, we found that KRAS^{G12V} degradation drove antitumor immunity by increasing CD8^{+} T cell activity. This was further manifested by a substantial increase of CD44^{high} effector CD8^{+} T cells, as well as CD69^{+} CD8^{+} and GzmB^{+} CD8^{+} cytotoxic T cells. Complementing these immune profiling data, our transcriptomic analysis revealed that KRAS^{G12V} degradation causes a strong inhibition of KRAS-dependent downstream signaling (E2F, mitosis, and cell cycle pathways) while also triggering robust immune response signaling.

Given our limited understanding of how KRAS^{G12V} impacts the lung TME, we conducted scRNA-seq analysis to identify global alterations in the TME following KRAS^{G12V} degradation. This analysis was complemented with further IHC and multiplex imaging staining. Our study uncovered several key observations and mechanisms of action on immune components. KRAS^{G12V} degradation upon dTAG^{V}-1 administration: (1) triggers the expansion and reduction of certain subtypes of tumor-infiltrating lymphoid (T and B cells) and myeloid cells (M1-like and M2-like

461 macrophages and DCs), (2) promotes a shift of naïve CD4$^+$ and CD8$^+$ T cells to effector/activated
462 T cells, and cytotoxic CD8$^+$ T cells, and (3) elicits an increase in the expression of an antitumor
463 cytotoxic gene signature. Supporting this, our *in vivo* T cell depletion assays support that a
464 functional immune system centered on CD8$^+$ T cells is required for the antitumor response
465 induced upon KRAS^{G12V} degradation. Additionally, our results also indicate that KRAS^{G12V}
466 degradation may promote tumor-associated macrophages towards M1-like antitumor phenotype
467 and affect different subtypes of B cells, which merits further investigation. Notably, there is
468 emerging interest in utilizing covalently modified peptide/MHC class I complexes as tumor-specific
469 neoantigens with KRAS^{G12C} inhibitors (62, 63). Future work is necessary to examine whether
470 KRAS degradation promotes the production of neoantigen peptides and whether this
471 phenomenon contributes to antitumor immunity. This research will also help experimentally rule
472 out the possibility of an FKBP12^{F36V} tag-induced immune response.

473 Our study also expands the use of the dTAG system for *in vivo* modeling. We and others have
474 shown that the dTAG system can be employed in xenograft models (27, 28, 37, 40, 64, 65) and
475 mouse models of embryonic development (38). An important consideration in these efforts is to
476 ensure that the tagged protein is functional and maintains the expected level of expression. One
477 limitation of tag-based systems is that the addition of a tag has the potential to alter protein stability
478 and half-life (66). In GEMMs, endogenous fusion with the FKBP12^{F36V}-tag may impact protein
479 stability and half-life, decreasing protein expression *in vivo* (39, 67). In our oncogene-induction
480 model, *FKBP12^{F36V}-KRAS^{G12V}* is driven by a PGK promoter. Studies in embryonic development
481 suggest that this may be target-specific (38) but future work is warranted to improve tagging
482 strategies to maintain protein stability to address this limitation. Furthermore, our oncogene-
483 induction model does not allow for the evaluation of the tolerability of systemic KRAS degradation.
484 GEMMs that employ the dTAG system such as those recently described for CDK2 and CDK5 will
485 prove to be highly complementary for evaluating toxicities from specific target protein loss (39).

486 In line with other studies, this work provides pre-clinical support that targeted degradation is a
487 powerful strategy to target mutant KRAS *in vivo* (21-25, 68). Recently, a clinical KRAS^{G12D}
488 degrader (ASP3082) was described to have potent antitumor activities in multiple *G12D*-driven
489 mouse models including pancreatic, colorectal, and NSCLC cancer (26). Currently, a phase 1
490 clinical trial is underway in patients with previously treated, locally advanced, or metastatic solid
491 tumors with *KRAS^{G12D}* mutation (NCT05382559). While it remains an open question whether
492 KRAS degradation will provide a benefit over inhibition, our work highlights the therapeutic
493 potential of targeted degradation of KRAS. It is worth noting that due to the current unavailability
494 of KRAS^{G12V}-specific inhibitors, a direct comparison of the immunological effects between
495 degrading KRAS^{G12V} and inhibiting KRAS^{G12V} is not yet experimentally achievable. When these
496 inhibitors become available, our mouse model will serve as an important platform for evaluating
497 the differential effects on downstream signaling, tumorigenesis, and TME alterations, allowing for
498 a comprehensive comparison of the responses to inhibitors and degraders. With the emergence
499 of pan-KRAS and RAS(ON) multi-selective inhibitors (69-72), it will also be interesting to evaluate
500 the immune responses triggered by these inhibitors and dTAG^V-1-mediated degradation in our
501 model.

502 Interestingly, a recent study showed that *Kras* oncogene ablation could prevent resistance to
503 KRAS inhibitors in advanced lung adenocarcinomas, supporting the potential benefit of protein
504 degradation (34). Supported by our prior cellular studies using the dTAG system studying
505 resistance mechanisms to targeted agents (28, 73), we expect that our model will enable the
506 identification of resistance mechanisms to KRAS disruption and the testing of drug combination
507 strategies *in vivo*. Future work will be necessary to evaluate drug combination approaches and to
508 extend our model to additional *KRAS* mutants and other *KRAS*-driven cancers. In summary, our
509 study demonstrates that degrading KRAS^{G12V} drives antitumor immunity and abolishes tumor

510   growth in lung cancer. Our work highlights the value of degradable model systems to understand
511   and advance targeted degradation strategies as cancer therapeutics.

Methods

Sex as a biological variable

Our study examined male and female animals, and similar findings are reported for both sexes.

Generation of FKBP12^{F36V}-KRAS^{G12V} transgenic mice

To generate FKBP12^{F36V}-KRAS^{G12V} mice that enable specific degradation by dTAG^V-1, we designed a targeting vector with a PGK promoter and Lox-Stop-Lox cassette, which allows the temporal and spatial control of gene expression as we previously described (43). *FKBP12^{F36V}-KRAS^{G12V}* complementary DNA was cloned into the targeting vector. The transgene expression is controlled by the stop cassette which can be removed by Cre recombinase. After the targeting vector was electroporated into embryonic stem (ES) cells, these cells were engineered to allow single-copy transgene insertion at the *Co1IA1* locus. ES clones that carry the *FKBP12^{F36V}-KRAS^{G12V}* transgene were selected, expanded, and used to inject into B6 blastocysts, which gave rise to chimeras. The chimeras were bred with wild-type B6 mice, and transgene-positive mice were genotyped/sequenced and expanded for experiments. From 6 to 8 weeks of age, mice were induced with adenovirus-SPC-Cre recombinase (Ad-Cre) by intranasal intubation to allow Cre-lox-mediated recombination.

In vivo studies

For NIH/3T3 KRAS^{G12V} or FKBP12^{F36V}-KRAS^{G12V} mouse model studies, 1 x 10^6 cells were injected into the flank of nude mice. Tumor growth was monitored and measured by caliper. For treatment studies using *FKBP12^{F36V}-KRAS^{G12V}* GEMMs, mice were evaluated by MRI imaging (Preclinical Imaging Laboratory, NYU Grossman School of Medicine and *in vivo* Imaging Facility, University of Pittsburgh UPMC Hillman Cancer Center) to quantify lung tumor burden before randomization and after drug treatment. Once the tumor volumes reached approximately 100 mm^3 (quantified by 3D-slicer using MRI images), the mice were then enrolled and randomized into either vehicle or dTAG^V-1 (35 mg/kg). For treatment studies using the PATU-8902 pancreatic cancer model, 1 x 10^6 cells were injected into the flank of nude mice. Tumor volumes were monitored and measured by caliper before randomization. Once tumor volumes reached approximately 100 mm^3, mice were randomized to treatment with either vehicle or dTAG^V-1 (35 mg/kg). For CD8$^+$ or CD4$^+$ T cell depletion studies, mice were injected intraperitoneally with either anti-CD8 antibody (400 mg, Bio X Cell, clone 2.43), or anti-CD4 (400 mg, Bio X Cell, clone GK1.5), or isotype control 48 and 24 h before beginning dTAG^V-1 treatment, and every 4 days thereafter.

Illustration tool

The schematic images were created with BioRender (BioRender.com).

Statistics

Statistical analyses were performed using GraphPad Prism v10 software and statistical significance was determined by $P < 0.05$. Data are presented as mean with SD unless otherwise specified. Statistical comparisons for two groups were performed using a two-tailed Student's *t*-test and multiple comparisons were performed using one-way ANOVA followed by post hoc Dunnett's test or Tukey's test unless otherwise specified (*$P < 0.05$, **$P < 0.01$, ***$P < 0.001$, ****$P < 0.0001$).

Study approval

All animal studies were reviewed and approved by the Institutional Animal Care and Use Committee at NYU Grossman School of Medicine and University of Pittsburgh School of Medicine. Both male and female mice were used, and all mice were maintained in accordance with NYU Grossman School of Medicine and University of Pittsburgh School of Medicine on the

care, welfare, and treatment of laboratory animals. All experiments met or exceeded the standards of the Association for the Assessment and Accreditation of Laboratory Animal Care, International, the U.S. Department of Health and Human Services, and all local and federal animal welfare laws.

Data availability

The accession number for the raw and processed data of bulk RNA sequencing and single-cell RNA sequencing generated and reported in this paper is GEO: GSE234472. All supporting data are provided in the Supporting Data Values file and available online as Supplemental Material.

Extended material and methods

Additional details on compounds, reagents, assays, and bioinformatic analysis are provided in the Supplemental Methods.

Author contributions

HZ, KKW, and BN conceptualized the study, designed the experiments, interpreted the data, wrote the manuscript, and supervised the study. DL, KG, JG, and SK performed most of the experiments, analyzed and interpreted the data, and contributed to writing the paper. YH performed bioinformatics analyses. ATO, CCK, YP, FS, HK, WMA, YL, TC, CT, MR, MM, DSL, JC, MSDP, JS, AC, JP, XS, ZZ, and MP conducted experiments, including *in vitro* assays in NIH/3T3 and AALE cells, multiplex imaging, MRI scan, dosing and IHC. FL, HH, SG, TZ, BH, BAN, WC, MEK, XW, JL, AHB, YL, XZ, TCB and NSG provided resources, analyzed, and interpreted the data. All authors reviewed the manuscript.

Acknowledgments

Figure Legends

Figure 1. Validation of targeted degradation of KRAS^{G12V} using the dTAG system. (A) Schematic of the dTAG system showing that dTAG^V-1 recruits the von Hippel-Lindau (VHL) E3 ubiquitin ligase to induce targeted degradation of FKBP12^{F36V}-KRAS^{G12V}. (B) Representative images of NIH/3T3 cells expressing GFP or FKBP12^{F36V}-GFP treated with DMSO, 500 nM dTAG^V-1, or 500 nM dTAG^V-1-NEG for 8 h. The scale bar represents 20 µm. Data is representative of n = 3 independent experiments. (C) Immunoblot analysis of HA to detect FKBP12^{F36V}-GFP or FKBP12^{F36V}-KRAS^{G12V}, KRAS, pMEK, MEK, and α-Tubulin of NIH/3T3 cells expressing GFP, FKBP12^{F36V}-GFP, KRAS^{G12V}, or FKBP12^{F36V}-KRAS^{G12V} treated with DMSO, 500 nM dTAG^V-1, or 500 nM dTAG^V-1-NEG for 8 h. Data is representative of n = 3 independent experiments. (D) Antiproliferation of NIH/3T3 cells expressing GFP, FKBP12^{F36V}-GFP, KRAS^{G12V}, or FKBP12^{F36V}-KRAS^{G12V} cultured as ultra-low adherent 3D-spheroid suspensions for 144 h. Data is presented as mean ± s.d. of n = 20 biologically independent samples and are representative of n = 3 independent experiments. RLU = Relative light units. (E) Tumor volume changes of NIH/3T3 cells expressing KRAS^{G12V} or FKBP12^{F36V}-KRAS^{G12V} that were subcutaneously injected into mice. Data is presented as mean ± SEM from n = 10 per group. (F) DMSO-normalized proliferation of NIH/3T3 cells expressing FKBP12^{F36V}-KRAS^{G12V} cultured as ultra-low adherent 3D-spheroid suspensions and treated with the indicated compounds for 120 h. Data is presented as mean ± s.d. of n = 4 biologically independent samples and are representative of n = 3 independent experiments. ****P < 0.0001 (D) and non-significant (NS) (D-E) by a one-way ANOVA with post hoc Tukey's test (D) or a two-tailed Student's t-test (E).

Figure 2. Establishing a GEMM for targeted degradation of KRAS^{G12V} in lung cancer. (A) Schematic showing the design of the *FKBP12^{F36V}-KRAS^{G12V}* GEMM. (B) Genomic sequencing confirmation of *KRAS^{G12V}* mutation in the GEMM. (C) MRI was performed to detect lung tumor nodules 12-14 weeks after adenovirus-carrying Cre recombinase delivery. (D) Representative images of hematoxylin and eosin (H&E) and immunohistochemistry (IHC) for TTF-1 of lung tumors from the *FKBP12^{F36V}-KRAS^{G12V}* GEMM. The scale bar represents 500 and 100 µm from top to bottom.

Figure 3. dTAG^V-1 effectively degrades KRAS^{G12V} and inhibits downstream signaling in a KRAS^{G12}-driven lung cancer GEMM. (A) Schematic showing the *in vivo* dosing schedule for evaluating target engagement and degradation. Mice were treated once daily with either vehicle or dTAG^V-1 (35 mg/kg) for 5 days. (B) Immunoblot analysis of HA to detect FKBP12^{F36V}-KRAS^{G12V}, pERK, ERK, and actin in lung tumor nodules after the indicated treatment and time from n = 3-5 per group. (C) Representative images of H&E and IHC staining for HA to detect FKBP12^{F36V}-KRAS^{G12V} and pERK of lung tumors after the indicated treatment from n = 3 per group. The scale bar represents 500, 200, 100 and 50 µm from top to bottom. (D) Quantification of HA to detect FKBP12^{F36V}-KRAS^{G12V} and pERK positive staining after the indicated treatment. Data is presented as mean ± s.d. of ten representative areas from n = 3 mice per group. (E) Representative images of IHC staining for Ki-67 and cleaved caspase-3 of lung tumors after the indicated treatment. The scale bar represents 100 and 50 µm for top and bottom. (F) Quantification of Ki-67 and cleaved caspase-3 positive staining after the indicated treatment. Data is presented as mean ± s.d. of ten representative areas from n = 3 mice per group. ****P < 0.0001 (D and F) by a two-tailed Student's t-test.

Figure 4. KRAS^{G12V} degradation abolishes tumor growth in *KRAS^{G12V}*-driven murine lung and pancreatic cancer models. (A) Schematic showing the *in vivo* dosing schedule for evaluating long-term dTAG^V-1 treatment. (B) Representative MRI scans (one vehicle and three dTAG^V-1 treated mice) of tumor baseline, 2 weeks, and 3 weeks after treatment initiation. The red arrowheads indicate lung tumors, and the red circles indicate the heart. (C) Waterfall plot and dot plot showing changes in tumor volume compared to baseline after 2 or 3/4 weeks of treatment.

646   Data is presented as mean ± s.d. from $n = 8$ per group. (**D**) Kaplan-Meier survival curve of
647   *FKBP12^{F36V}-KRAS^{G12V}* lung cancer mice after long-term treatment with vehicle or dTAG^V-1 from
648    $n = 9$ per group. (**E**) Tumor volume changes of PATU-8902 FKBP12^{F36V}-KRAS^{G12V}; *KRAS$^{-/-}$* cells
649   that were subcutaneously injected into mice and treated with vehicle or dTAG^V-1. Data is
650   presented as mean ± SEM from $n = 12$ per group. (**F**) Representative pancreatic tumors after the
651   indicated treatment. ****$P < 0.0001$ by a one-way ANOVA with post hoc Dunnett's test (**C**) and a
652   two-tailed Student's *t*-test (**E**).

653   **Figure 5. KRAS^{G12V} degradation increases CD8$^+$ T activity in a *KRAS^{G12V}*-driven lung cancer**
654   **GEMM.** (**A**) Schematic showing the experimental design for immune profiling. After confirming
655   tumor burden by MRI, mice were randomized and treated once daily with either vehicle or dTAG^V-
656   1 (35 mg/kg) for 5 days. Tumor nodules were then collected, and tumor-infiltrating lymphocytes
657   were analyzed by flow cytometry. (**B** and **C**) Frequencies of CD44$^+$ CD8$^+$ T cells and CD62L$^+$
658   CD8$^+$ T cells from $n = 5$ per group. Data is presented as mean ± SEM (**C**). (**D** and **E**) Frequencies
659   of CD69$^+$ CD8$^+$ T cells and GZMB$^+$ CD8$^+$ T cells from $n = 5$ per group. Data is presented as mean
660   ± SEM (**E**). *$P < 0.05$ and **$P < 0.01$ (**C** and **E**) by a two-tailed Student's *t*-test.

661   **Figure 6. Single-cell RNA-seq reveals KRAS^{G12V} degradation reprograms the TME to**
662   **promote antitumor immunity in a *KRAS^{G12V}*-driven lung cancer GEMM.** (**A**) UMAP plot
663   showing identified cell populations including tumor cells, immune cells, and fibroblasts. (**B**) UMAP
664   plots showing the expression of cell-type specific marker genes. (**C**) Percentage of cells in TME
665   of annotated clusters in response to the indicated treatments. (**D**) UMAP plot showing identified
666   cell subsets in T cell population. (**E**) UMAP plots show the expression of selected marker genes.
667   (**F**) Percentage of cells in the annotated T cell subsets in response to the indicated treatments.

668   **Figure 7. Antitumor immunity by KRAS^{G12V} degradation is partly dependent on CD8$^+$ T cells**
669   **in a *KRAS^{G12V}*-driven lung cancer GEMM.** (**A** and **B**) Representative multiplex IF images
670   showing (**A**) tumor infiltrating CD3$^+$ T cells, Foxp3$^+$ Treg cells and (**B**) CD19$^+$ B cells in response
671   to indicated treatment. The same samples are presented in **A** and **B**. The scale bar represents
672   50 and 10 µm from left to right, respectively. (**C**) Quantification of CD3$^+$ T cells, Foxp3$^+$ Treg cells
673   and CD19$^+$ B cells in response to the indicated treatment. Data is presented as mean ± s.d. of ten
674   representative areas from $n = 3$ mice per group. (**D**) Representative MRI scans of lung tumors at
675   baseline and 2 weeks in response to indicated treatment. The red arrowheads indicate lung
676   tumors. (**E** and **F**) Waterfall plot (**E**) and dot plot (**F**) showing changes in tumor volume compared
677   to baseline after 2 weeks of treatment. Data is presented as mean ± s.d. from $n = 4$-6 per group.
678   **$P < 0.01$, ***$P < 0.001$, ****$P < 0.0001$ and non-significant (NS) by a two-tailed Student's *t*-test
679   (**C**) and a one-way ANOVA with post hoc Tukey's test (**F**).

References

1. Siegel R L, et al. Cancer statistics, 2019. *CA Cancer J Clin.* 2019;69(1):7-34.
2. Cheng L, et al. Molecular pathology of lung cancer: key to personalized medicine. *Mod Pathol.* 2012;25(3):347-369.
3. Scheffler M, et al. K-ras mutation subtypes in NSCLC and associated co-occuring mutations in other oncogenic pathways. *J Thorac Oncol.* 2019;14(4):606-616.
4. Janes M R, et al. Targeting KRAS mutant cancers with a covalent G12C-specific inhibitor. *Cell.* 2018;172(3):578-589 e517.
5. Lanman B A, et al. Discovery of a covalent inhibitor of KRAS^{G12C} (AMG 510) for the treatment of solid tumors. *J Med Chem.* 2020;63(1):52-65.
6. Canon J, et al. The clinical KRAS(G12C) inhibitor AMG 510 drives anti-tumour immunity. *Nature.* 2019;575(7781):217-223.
7. Hallin J, et al. The KRAS^{G12C} inhibitor MRTX849 provides insight toward therapeutic susceptibility of KRAS-mutant cancers in mouse models and patients. *Cancer Discov.* 2020;10(1):54-71.
8. Jänne P A, et al. KRYSTAL-1: activity and safety of adagrasib (MRTX849) in advanced/metastatic non-small cell lung cancer (NSCLC) harboring KRAS G12C mutation. *ENA.* 2020.
9. Hong D S, et al. KRAS^{G12C} inhibition with sotorasib in advanced solid tumors. *N Engl J Med.* 2020;383(13):1207-1217.
10. de Langen A J, et al. Sotorasib versus docetaxel for previously treated non-small-cell lung cancer with KRAS^{G12C} mutation: a randomised, open-label, phase 3 trial. *Lancet.* 2023;401(10378):733-746.
11. Zhao Y, et al. Diverse alterations associated with resistance to KRAS(G12C) inhibition. *Nature.* 2021;599(7886):679-683.
12. Xue J Y, et al. Rapid non-uniform adaptation to conformation-specific KRAS(G12C) inhibition. *Nature.* 2020;577(7790):421-425.
13. Kim D, et al. Targeting KRAS(G12C): from inhibitory mechanism to modulation of antitumor effects in patients. *Cell.* 2020;183(4):850-859.
14. Sakamoto K M, et al. Protacs: chimeric molecules that target proteins to the Skp1-Cullin-F box complex for ubiquitination and degradation. *Proc Natl Acad Sci U S A.* 2001;98(15):8554-8559.
15. Burslem G M, and Crews C M. Proteolysis-targeting chimeras as therapeutics and tools for biological discovery. *Cell.* 2020;181(1):102-114.
16. Bekes M, et al. PROTAC targeted protein degraders: the past is prologue. *Nat Rev Drug Discov.* 2022;21(3):181-200.
17. Chirnomas D, et al. Protein degraders enter the clinic - a new approach to cancer therapy. *Nat Rev Clin Oncol.* 2023;20(4):265-278.
18. Bondeson D P, et al. Catalytic in vivo protein knockdown by small-molecule PROTACs. *Nat Chem Biol.* 2015;11(8):611-617.
19. Burslem G M, et al. The advantages of targeted protein degradation over inhibition: an RTK case study. *Cell Chem Biol.* 2018;25(1):67-77 e63.
20. Koide E, et al. Development and characterization of selective FAK inhibitors and PROTACs with in vivo activity. *Chembiochem.* 2023:e202300141.
21. Zeng M, et al. Exploring targeted degradation strategy for oncogenic KRAS^{G12C}. *Cell Chem Biol.* 2020;27(1):19-31 e16.
22. Bond M J, et al. Targeted degradation of oncogenic KRAS^{G12C} by VHL-recruiting PROTACs. *ACS Cent Sci.* 2020;6(8):1367-1375.
23. Popow J, et al. Targeting cancer with small-molecule pan-KRAS degraders. *Science.* 2024;385(6715):1338-1347.

730   24.   Bery N, et al. A potent KRAS macromolecule degrader specifically targeting tumours with
731   mutant KRAS. *Nat Commun.* 2020;11(1):3233.

732   25.   Yang J, et al. A pan-KRAS degrader for the treatment of KRAS-mutant cancers. *Cell*
733   *Discov.* 2024;10(1):70.

734   26.   Nagashima T, et al. Abstract 5735: Novel KRAS G12D degrader ASP3082 demonstrates
735   in vivo, dose-dependent KRAS degradation, KRAS pathway inhibition, and antitumor
736   efficacy in multiple KRAS G12D-mutated cancer models. *Cancer Research.*
737   2023;83(7_Supplement):5735.

738   27.   Nabet B, et al. The dTAG system for immediate and target-specific protein degradation.
739   *Nat Chem Biol.* 2018;14(5):431-441.

740   28.   Nabet B, et al. Rapid and direct control of target protein levels with VHL-recruiting dTAG
741   molecules. *Nat Commun.* 2020;11(1):4687.

742   29.   Ferguson F M, et al. Discovery of a selective inhibitor of doublecortin like kinase 1. *Nat*
743   *Chem Biol.* 2020;16(6):635-643.

744   30.   Nabet B. Charting a new path towards degrading every protein. *Chembiochem.*
745   2021;22(3):483-484.

746   31.   Nabet B, et al. Protein homeostasis in drug discovery: a chemical biology perspective.
747   *Wiley.* 2022:447-464.

748   32.   Guerra C, et al. Tumor induction by an endogenous K-ras oncogene is highly dependent
749   on cellular context. *Cancer Cell.* 2003;4(2):111-120.

750   33.   Sanclemente M, et al. c-RAF ablation induces regression of advanced Kras/Trp53 mutant
751   lung adenocarcinomas by a mechanism independent of MAPK signaling. *Cancer Cell.*
752   2018;33(2):217-228 e214.

753   34.   Salmon M, et al. Kras oncogene ablation prevents resistance in advanced lung
754   adenocarcinomas. *J Clin Invest.* 2023;133(7).

755   35.   Drosten M, et al. Genetically engineered mouse models of K-Ras-driven lung and
756   pancreatic tumors: validation of therapeutic targets. *Cold Spring Harb Perspect Med.*
757   2018;8(5).

758   36.   Jaeger M G, and Winter G E. Fast-acting chemical tools to delineate causality in
759   transcriptional control. *Mol Cell.* 2021;81(8):1617-1630.

760   37.   Bilal F, et al. The transcription factor SLUG uncouples pancreatic cancer progression from
761   the RAF-MEK1/2-ERK1/2 pathway. *Cancer Res.* 2021;81(14):3849-3861.

762   38.   Abuhashem A, et al. Rapid and efficient degradation of endogenous proteins in vivo
763   identifies stage-specific roles of RNA Pol II pausing in mammalian development. *Dev Cell.*
764   2022;57(8):1068-1080 e1066.

765   39.   Yenerall P, et al. Use of the dTAG system in vivo to degrade CDK2 and CDK5 in adult
766   mice and explore potential safety liabilities. *Toxicol Sci.* 2023;194(1):53-69.

767   40.   Lin S, et al. An *in vivo* CRISPR screening platform for prioritizing therapeutic targets in
768   AML. *Cancer Discov.* 2022;12(2):432-449.

769   41.   Vichas A, et al. Integrative oncogene-dependency mapping identifies RIT1 vulnerabilities
770   and synergies in lung cancer. *Nat Commun.* 2021;12(1):4789.

771   42.   Lo A, et al. Multiomic characterization of oncogenic signaling mediated by wild-type and
772   mutant RIT1. *Sci Signal.* 2021;14(711):eabc4520.

773   43.   Akbay E A, et al. Interleukin-17A promotes lung tumor progression through neutrophil
774   attraction to tumor sites and mediating resistance to PD-1 blockade. *J Thorac Oncol.*
775   2017;12(8):1268-1279.

776   44.   Jackson E L, et al. Analysis of lung tumor initiation and progression using conditional
777   expression of oncogenic K-ras. *Genes Dev.* 2001;15(24):3243-3248.

778   45.   Briere D M, et al. The KRAS^{G12C} inhibitor MRTX849 reconditions the tumor immune
779   microenvironment and sensitizes tumors to checkpoint inhibitor therapy. *Mol Cancer Ther.*
780   2021;20(6):975-985.

781 46. Molina-Arcas M, and Downward J. Exploiting the therapeutic implications of KRAS
782   inhibition on tumor immunity. *Cancer Cell.* 2024;42(3):338-357.
783 47. Pan Y, et al. Tumor-associated macrophages in tumor immunity. *Front Immunol.*
784   2020;11:583084.
785 48. Wang S, et al. Targeting M2-like tumor-associated macrophages is a potential therapeutic
786   approach to overcome antitumor drug resistance. *NPJ Precis Oncol.* 2024;8(1):31.
787 49. Chen J, et al. Single-cell transcriptome and antigen-immunoglobin analysis reveals the
788   diversity of B cells in non-small cell lung cancer. *Genome Biol.* 2020;21(1):152.
789 50. Zilionis R, et al. Single-cell transcriptomics of human and mouse lung cancers reveals
790   conserved myeloid populations across individuals and species. *Immunity.*
791   2019;50(5):1317-1334 e1310.
792 51. Jablonski K A, et al. Novel markers to delineate murine M1 and M2 macrophages. *PLoS*
793   *One.* 2015;10(12):e0145342.
794 52. Bod L, et al. B-cell-specific checkpoint molecules that regulate anti-tumour immunity.
795   *Nature.* 2023;619(7969):348-356.
796 53. Morgan D, and Tergaonkar V. Unraveling B cell trajectories at single cell resolution.
797   *Trends Immunol.* 2022;43(3):210-229.
798 54. Lambrechts D, et al. Phenotype molding of stromal cells in the lung tumor
799   microenvironment. *Nat Med.* 2018;24(8):1277-1289.
800 55. Li H, et al. Fc Receptor-like 5 expression distinguishes two distinct subsets of human
801   circulating tissue-like memory B cells. *J Immunol.* 2016;196(10):4064-4074.
802 56. Kim C C, et al. FCRL5^{+} memory B cells exhibit robust recall responses. *Cell Rep.*
803   2019;27(5):1446-1460 e1444.
804 57. Paiva S L, and Crews C M. Targeted protein degradation: elements of PROTAC design.
805   *Curr Opin Chem Biol.* 2019;50:111-119.
806 58. Lee J K, et al. Comprehensive pan-cancer genomic landscape of KRAS altered cancers
807   and real-world outcomes in solid tumors. *NPJ Precis Oncol.* 2022;6(1):91.
808 59. Fernandez Montes A, et al. The frequency of specific KRAS mutations, and their impact
809   on treatment choice and survival, in patients with metastatic colorectal cancer. *Oncologist.*
810   2023;28(10):e902-e9.
811 60. Skoulidis F, et al. Sotorasib for lung cancers with *KRAS p.*G12C mutation. *N Engl J Med.*
812   2021;384(25):2371-2381.
813 61. Janne P A, et al. Adagrasib in non-small-cell lung cancer harboring a *KRAS^{G12C}* mutation.
814   *N Engl J Med.* 2022;387(2):120-131.
815 62. Zhang Z, et al. A covalent inhibitor of K-Ras(G12C) induces MHC class I presentation of
816   haptenated peptide neoepitopes targetable by immunotherapy. *Cancer Cell.*
817   2022;40(9):1060-1069 e1067.
818 63. Hattori T, et al. Creating MHC-restricted neoantigens with covalent inhibitors that can be
819   targeted by immune therapy. *Cancer Discov.* 2023;13(1):132-145.
820 64. Nirala B K, et al. MYC regulates CSF-1 expression via microRNA 17/20a to modulate
821   tumor-associated macrophages in osteosarcoma. *JCI Insight.* 2023.
822 65. Radko-Juettner S, et al. Targeting DCAF5 suppresses SMARCB1-mutant cancer by
823   stabilizing SWI/SNF. *Nature.* 2024;628(8007):442-449.
824 66. Vetma V, et al. Confounding factors in targeted degradation of short-lived proteins. *ACS*
825   *Chem Biol.* 2024;19(7):1484-1494.
826 67. Mehta S, et al. Temporal resolution of gene derepression and proteome changes upon
827   PROTAC-mediated degradation of BCL11A protein in erythroid cells. *Cell Chem Biol.*
828   2022;29(8):1273-1287 e1278.
829 68. Yang F, et al. Efficient targeted oncogenic KRAS^{G12C} degradation via first reversible-
830   covalent PROTAC. *Eur J Med Chem.* 2022;230:114088.

831 69. Kim D, et al. Pan-KRAS inhibitor disables oncogenic signalling and tumour growth. *Nature.*
832   2023;619(7968):160-166.
833 70. Holderfield M, et al. Concurrent inhibition of oncogenic and wild-type RAS-GTP for cancer
834   therapy. *Nature.* 2024;629(8013):919-926.
835 71. Wasko U N, et al. Tumour-selective activity of RAS-GTP inhibition in pancreatic cancer.
836   *Nature.* 2024;629(8013):927-936.
837 72. Schulze C J, et al. Chemical remodeling of a cellular chaperone to target the active state
838   of mutant KRAS. *Science.* 2023;381(6659):794-799.
839 73. Sulahian R, et al. Synthetic lethal interaction of SHOC2 depletion with MEK inhibition in
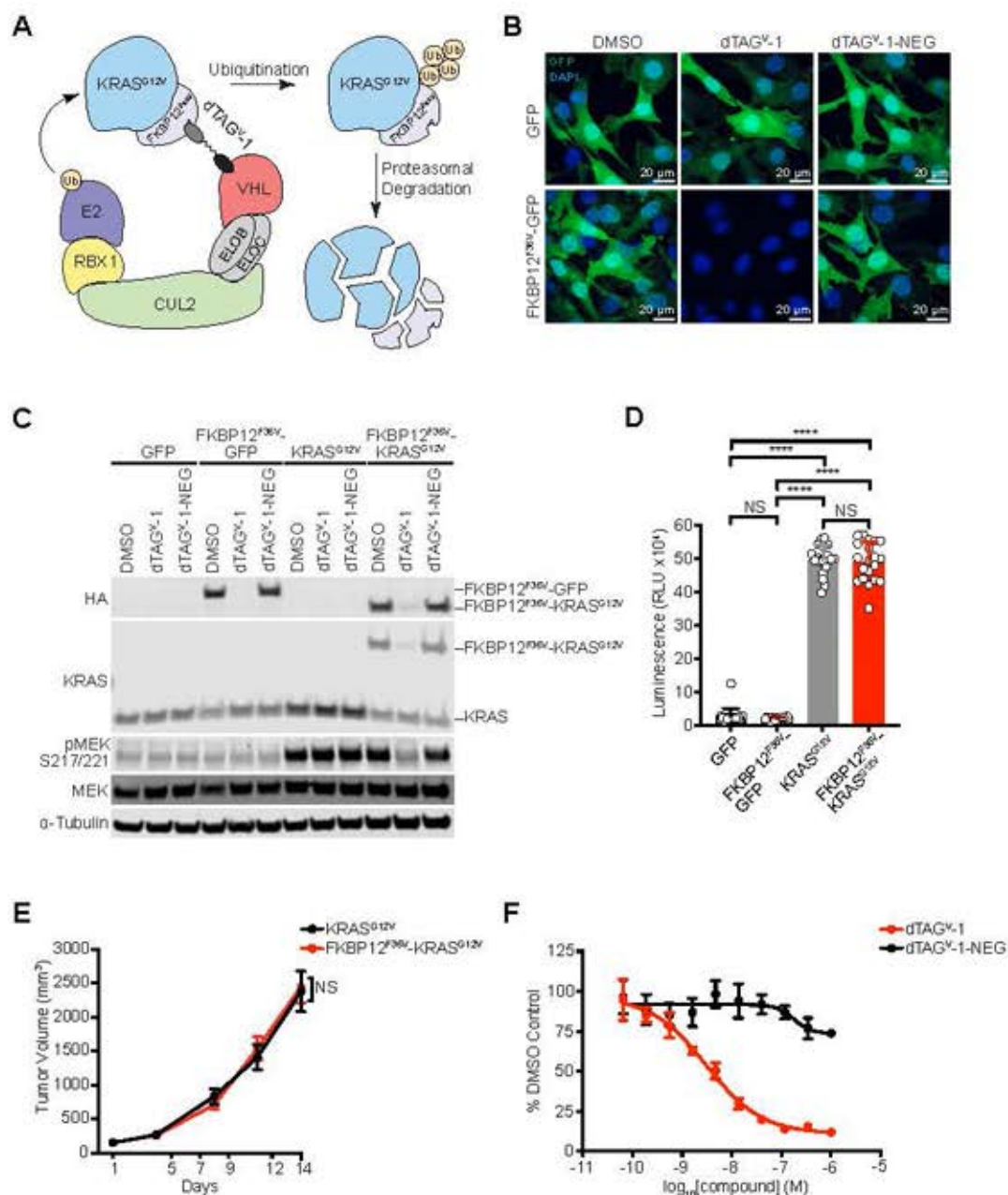840   RAS-driven cancers. *Cell Rep.* 2019;29(1):118-134 e118.
841
842

Figure 1. Validation of targeted degradation of KRAS^G12V using the dTAG system. (A) Schematic of the dTAG system showing that dTAG^V-1 recruits the von Hippel-Lindau (VHL) E3 ubiquitin ligase to induce targeted degradation of FKBP12^F36V-KRAS^G12V. **(B)** Representative images of NIH/3T3 cells expressing GFP or FKBP12^F36V-GFP treated with DMSO, 500 nM dTAG^V-1, or 500 nM dTAG^V-1-NEG for 8 h. The scale bar represents 20 μm. Data is representative of *n* = 3 independent experiments. **(C)** Immunoblot analysis of HA to detect FKBP12^F36V-GFP or FKBP12^F36V-KRAS^G12V, KRAS, pMEK, MEK, and α-Tubulin of NIH/3T3 cells expressing GFP, FKBP12^F36V-GFP, KRAS^G12V, or FKBP12^F36V-KRAS^G12V treated with DMSO, 500 nM dTAG^V-1, or 500 nM dTAG^V-1-NEG for 8 h. Data is representative of *n* = 3 independent experiments. **(D)** Antiproliferation of NIH/3T3 cells expressing GFP, FKBP12^F36V-GFP, KRAS^G12V, or FKBP12^F36V-KRAS^G12V cultured as ultra-low adherent 3D-spheroid suspensions for 144 h. Data is presented as mean ± s.d. of *n* = 20 biologically independent samples and are representative of *n* = 3 independent experiments. RLU = Relative light units. **(E)** Tumor volume changes of NIH/3T3 cells expressing KRAS^G12V or FKBP12^F36V-KRAS^G12V that were subcutaneously injected into mice. Data is presented as mean ± SEM from *n* = 10 per group. **(F)** DMSO-normalized proliferation of NIH/3T3 cells expressing FKBP12^F36V-KRAS^G12V cultured as ultra-low adherent 3D-spheroid suspensions and treated with the indicated compounds for 120 h. Data is presented as mean ± s.d. of *n* = 4 biologically independent samples and are representative of *n* = 3 independent experiments. ****P < 0.0001 **(D)** and non-significant (NS) **(D-E)** by a one-way ANOVA with post hoc Tukey's test **(D)** or a two-tailed Student's *t*-test **(E)**.
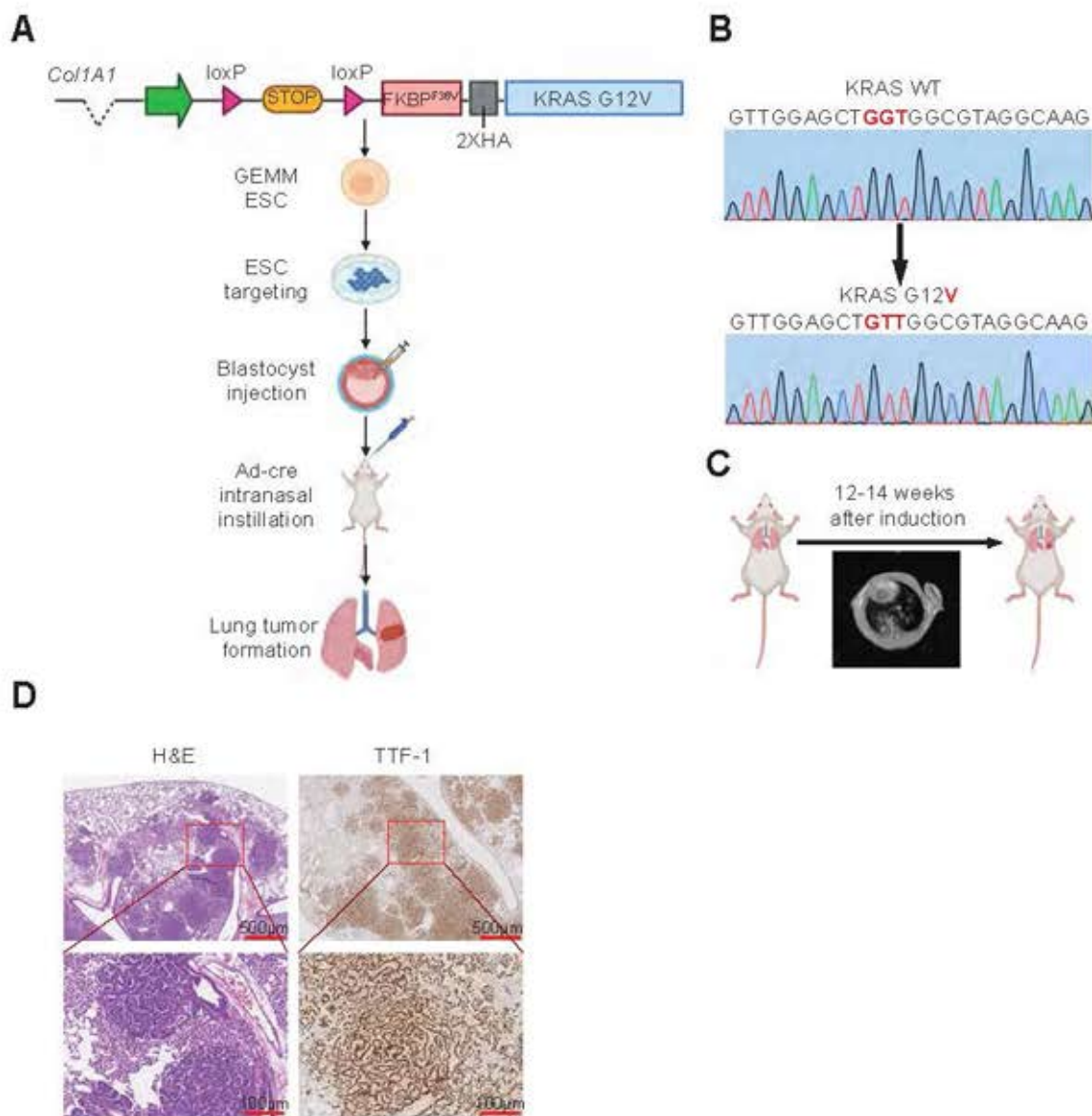
Figure 2. Establishing a GEMM for targeted degradation of KRAS^{G12V} in lung cancer. (**A**) Schematic showing the design of the *FKBP12^{F36V}-KRAS^{G12V}* GEMM. (**B**) Genomic sequencing confirmation of *KRAS^{G12V}* mutation in the GEMM. (**C**) MRI was performed to detect lung tumor nodules 12-14 weeks after adenovirus-carrying Cre recombinase delivery. (**D**) Representative images of hematoxylin and eosin (H&E) and immunohistochemistry (IHC) for TTF-1 of lung tumors from the *FKBP12^{F36V}-KRAS^{G12V}* GEMM. The scale bar represents 500 and 100 µm from top to bottom.
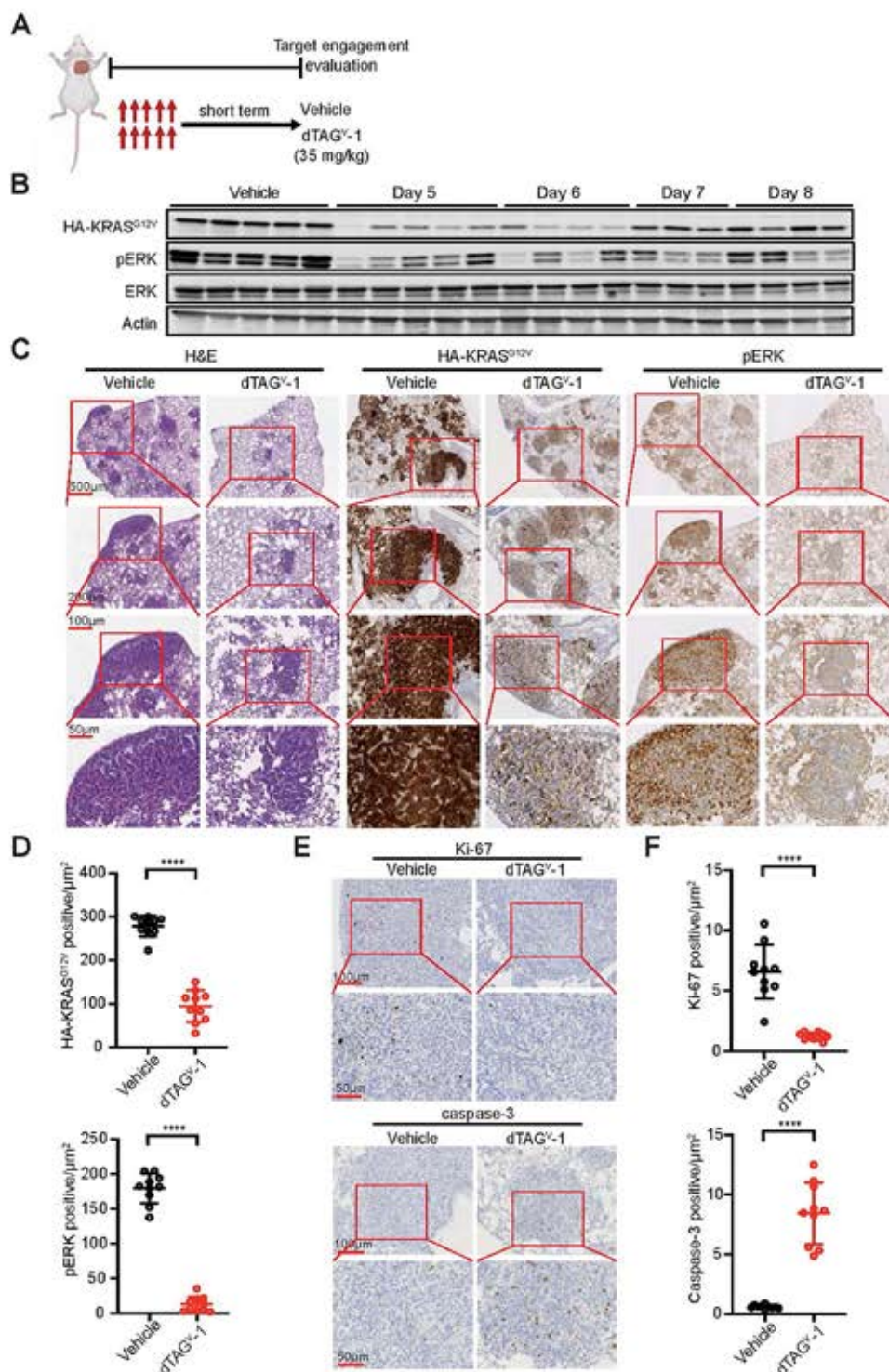
Figure 3. dTAG^V-1 effectively degrades KRAS^{G12V} and inhibits downstream signaling in a KRAS^{G12}-driven lung cancer GEMM. (**A**) Schematic showing the *in vivo* dosing schedule for evaluating target engagement and degradation. Mice were treated once daily with either vehicle or dTAG^V-1 (35 mg/kg) for 5 days. (**B**) Immunoblot analysis of HA to detect FKBP12^{F36V}-KRAS^{G12V}, pERK, ERK, and actin in lung tumor nodules after the indicated treatment and time from n = 3-5 per group. (**C**) Representative images of H&E and IHC staining for HA to detect FKBP12^{F36V}-KRAS^{G12V} and pERK of lung tumors after the indicated treatment from n = 3 per group. The scale bar represents 500, 200, 100 and 50 μm from top to bottom. (**D**) Quantification of HA to detect FKBP12^{F36V}-KRAS^{G12V} and pERK positive staining after the indicated treatment. Data is presented as mean ± s.d. of ten representative areas from n = 3 mice per group. (**E**) Representative images of IHC staining for Ki-67 and cleaved caspase-3 of lung tumors after the indicated treatment. The scale bar represents 100 and 50 μm for top and bottom. (**F**) Quantification of Ki-67 and cleaved caspase-3 positive staining after the indicated treatment. Data is presented as mean ± s.d. of ten representative areas from n = 3 mice per group. ****P < 0.0001 (**D** and **F**) by a two-tailed Student's *t*-test.
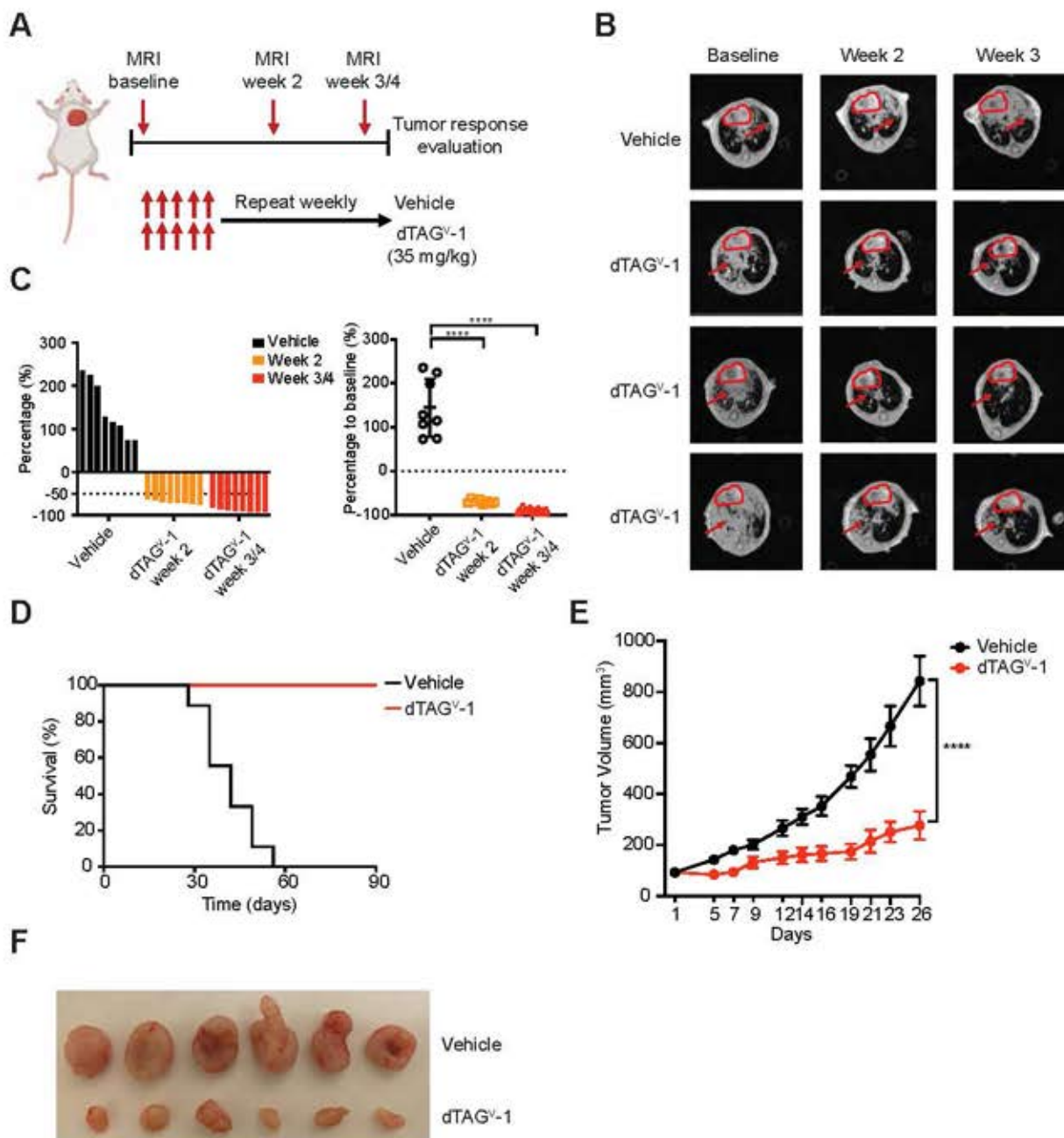
Figure 4. KRAS^G12V degradation abolishes tumor growth in *KRAS^G12V*-driven murine lung and pancreatic cancer models. (**A**) Schematic showing the *in vivo* dosing schedule for evaluating long-term dTAG^V-1 treatment. (**B**) Representative MRI scans (one vehicle and three dTAG^V-1 treated mice) of tumor baseline, 2 weeks, and 3 weeks after treatment initiation. The red arrowheads indicate lung tumors, and the red circles indicate the heart. (**C**) Waterfall plot and dot plot showing changes in tumor volume compared to baseline after 2 or 3/4 weeks of treatment. Data is presented as mean ± s.d. from $n = 8$ per group. (**D**) Kaplan-Meier survival curve of *FKBP12^F36V-KRAS^G12V* lung cancer mice after long-term treatment with vehicle or dTAG^V-1 from $n = 9$ per group. (**E**) Tumor volume changes of PATU-8902 FKBP12^F36V-KRAS^G12V; *KRAS^-/-* cells that were subcutaneously injected into mice and treated with vehicle or dTAG^V-1. Data is presented as mean ± SEM from $n = 12$ per group. (**F**) Representative pancreatic tumors after the indicated treatment. ****$P < 0.0001$ by a one-way ANOVA with post hoc Dunnett's test (**C**) and a two-tailed Student's *t*-test (**E**).
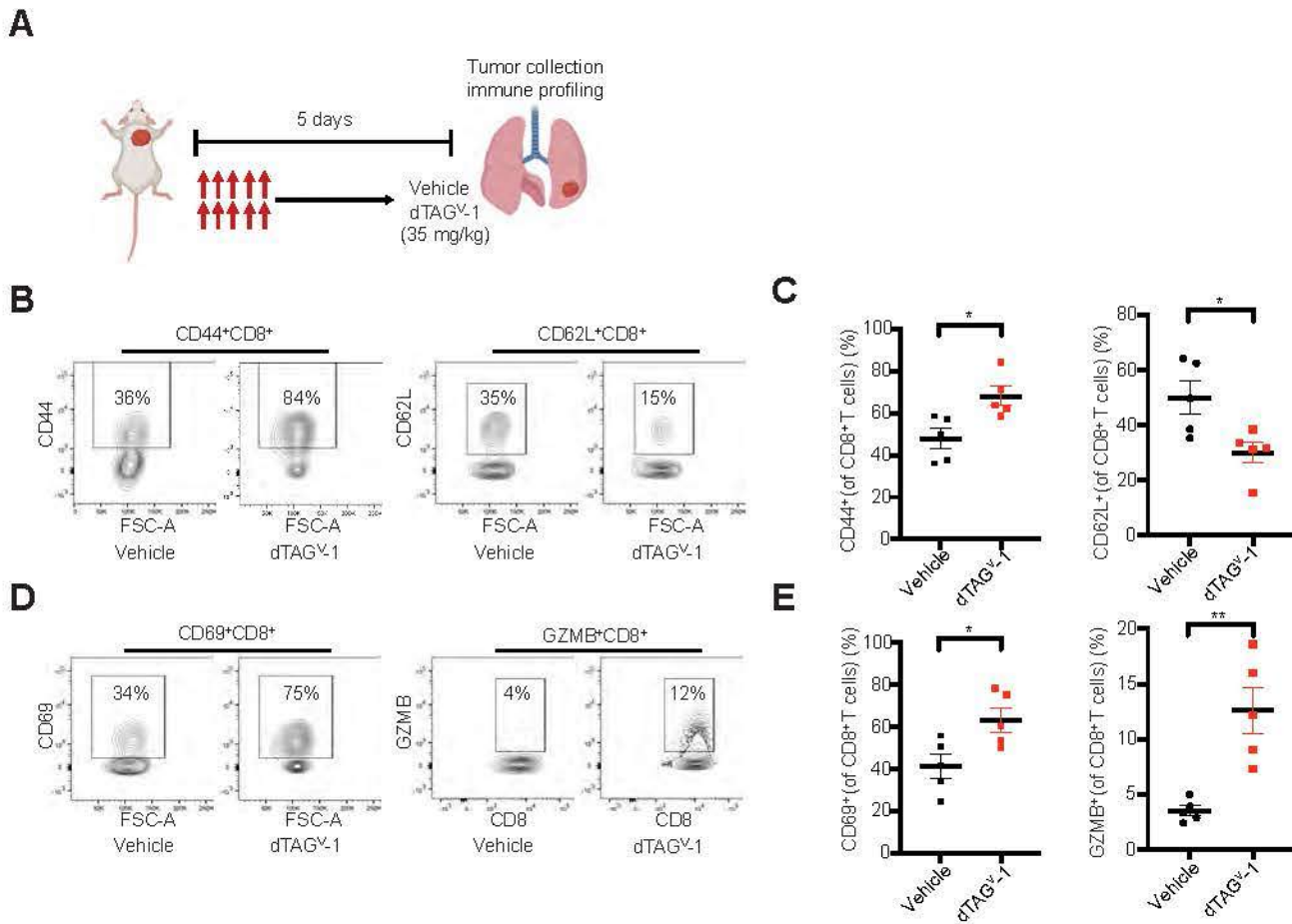
Figure 5. KRAS^G12V degradation increases CD8⁺ T activity in a *KRAS^G12V*-driven lung cancer GEMM. (**A**) Schematic showing the experimental design for immune profiling. After confirming tumor burden by MRI, mice were randomized and treated once daily with either vehicle or dTAG^V-1 (35 mg/kg) for 5 days. Tumor nodules were then collected, and tumor-infiltrating lymphocytes were analyzed by flow cytometry. (**B** and **C**) Frequencies of CD44⁺ CD8⁺ T cells and CD62L⁺ CD8⁺ T cells from $n = 5$ per group. Data is presented as mean ± SEM (**C**). (**D** and **E**) Frequencies of CD69⁺ CD8⁺ T cells and GZMB⁺ CD8⁺ T cells from $n = 5$ per group. Data is presented as mean ± SEM (**E**). *$P < 0.05$ and **$P < 0.01$ (**C** and **E**) by a two-tailed Student's *t*-test.
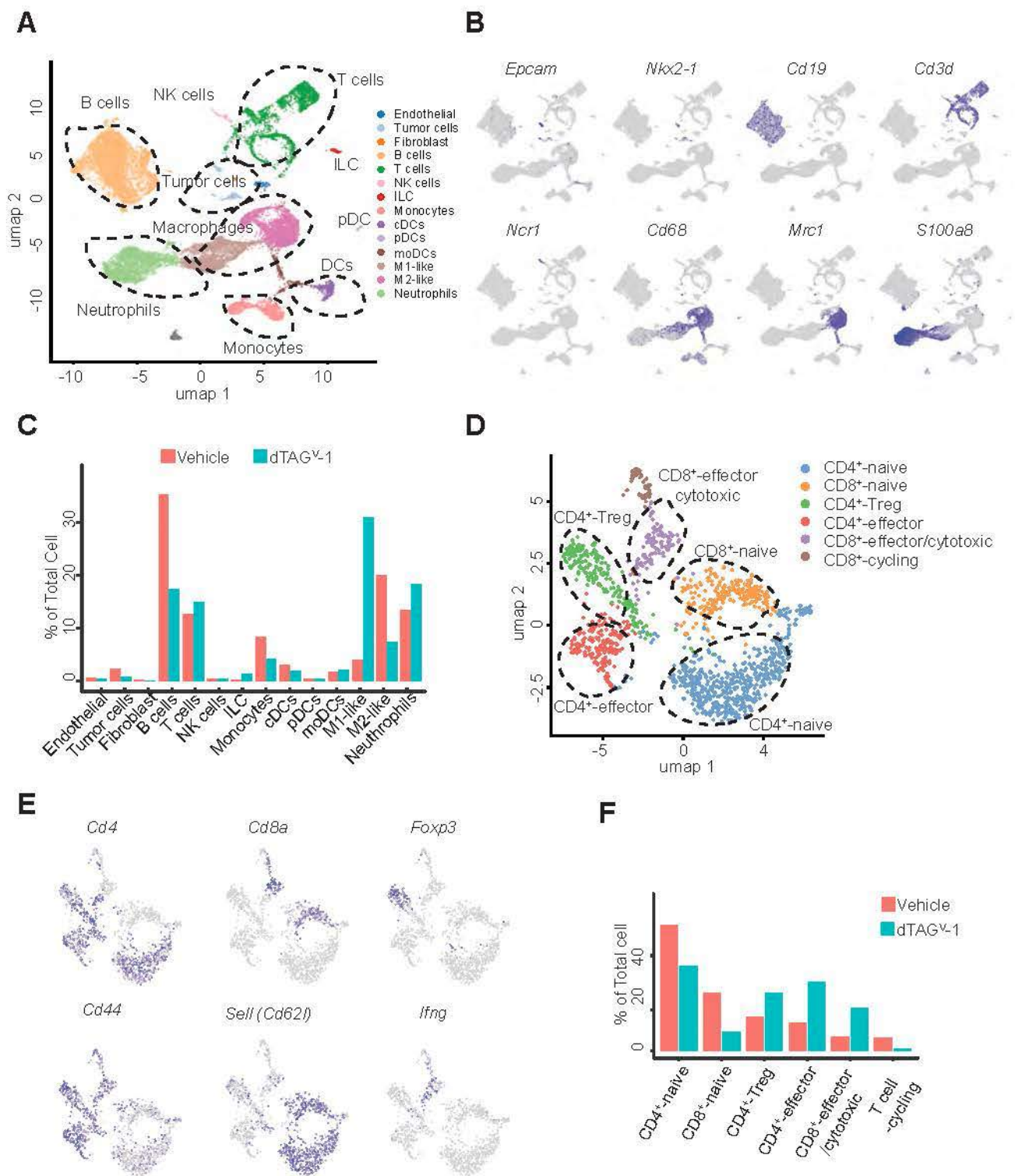
Figure 6. Single-cell RNA-seq reveals KRAS^{G12V} degradation reprograms the TME to promote antitumor immunity in a *KRAS^{G12V}*-driven lung cancer GEMM. (**A**) UMAP plot showing identified cell populations including tumor cells, immune cells, and fibroblasts. (**B**) UMAP plots showing the expression of cell-type specific marker genes. (**C**) Percentage of cells in TME of annotated clusters in response to the indicated treatments. (**D**) UMAP plot showing identified cell subsets in T cell population. (**E**) UMAP plots show the expression of selected marker genes. (**F**) Percentage of cells in the annotated T cell subsets in response to the indicated treatments.
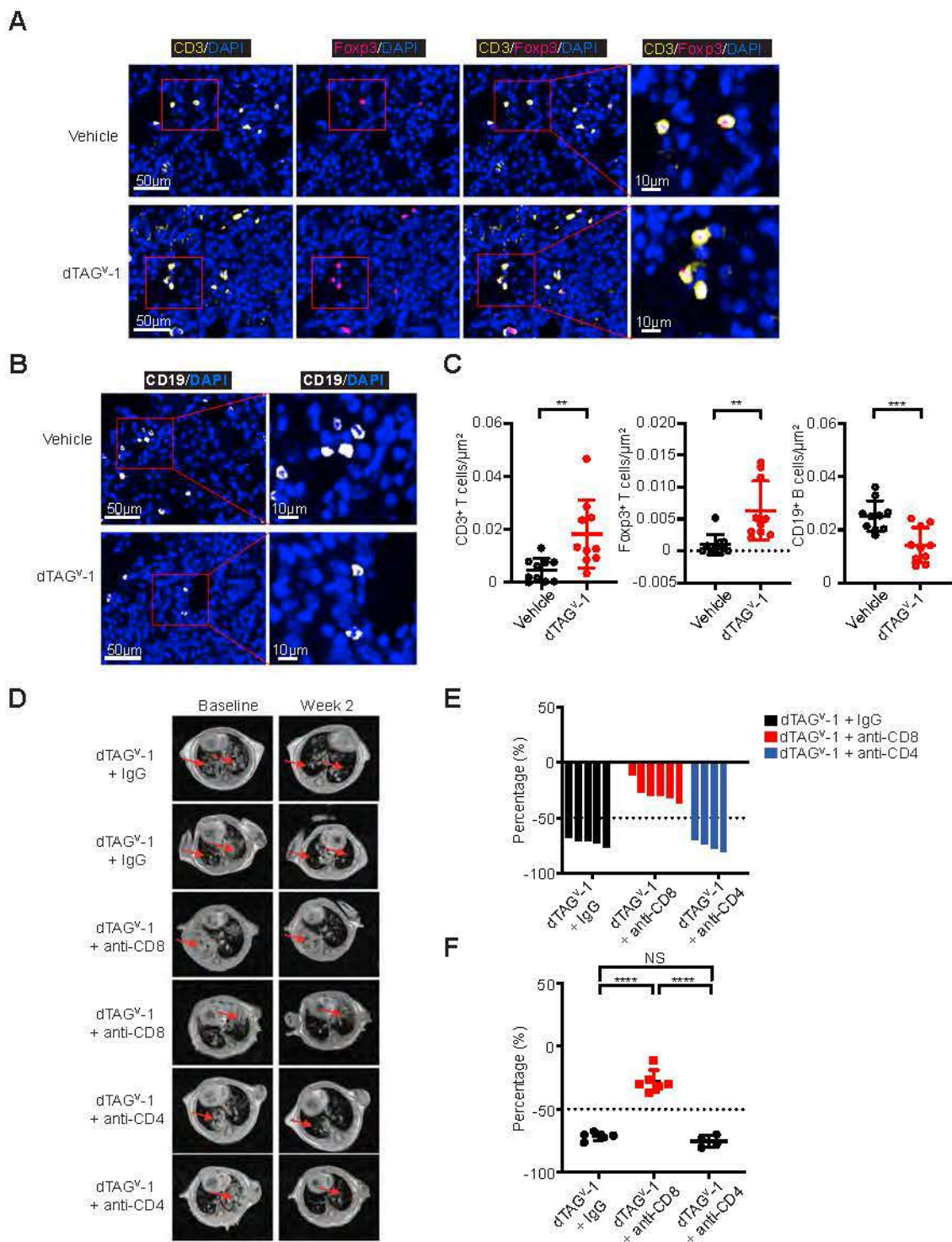
Figure 7. Antitumor immunity by KRAS^{G12V} degradation is partly dependent on CD8$^+$ T cells in a *KRAS^{G12V}*-driven lung cancer GEMM. (A and **B)** Representative multiplex IF images showing **(A)** tumor infiltrating CD3$^+$ T cells, Foxp3$^+$ Treg cells and **(B)** CD19$^+$ B cells in response to indicated treatment. The same samples are presented in **A** and **B**. The scale bar represents 50 and 10 μm from left to right, respectively. **(C)** Quantification of CD3$^+$ T cells, Foxp3$^+$ Treg cells and CD19$^+$ B cells in response to the indicated treatment. Data is presented as mean ± s.d. of ten representative areas from $n = 3$ mice per group. **(D)** Representative MRI scans of lung tumors at baseline and 2 weeks in response to indicated treatment. The red arrowheads indicate lung tumors. **(E** and **F)** Waterfall plot **(E)** and dot plot **(F)** showing changes in tumor volume compared to baseline after 2 weeks of treatment. Data is presented as mean ± s.d. from $n = 4$-6 per group. **$P < 0.01$, ***$P < 0.001$, ****$P < 0.0001$ and non-significant (NS) by a two-tailed Student's *t*-test **(C)** and a one-way ANOVA with post hoc Tukey's test **(F)**.